

WL-TR-97-4107

**MECHANICS OF BRITTLE-MATRIX COMPOSITES**

R. Y. Kim

University of Dayton Research Institute  
300 College Park Avenue  
Dayton, OH 45469-0168



**AUGUST 1997**

Final Report for Period 15 September 1995 - 2 June 1997

Approved for public release; distribution unlimited.

19980514 099

MATERIALS DIRECTORATE  
WRIGHT LABORATORY  
AIR FORCE MATERIEL COMMAND  
WRIGHT-PATTERSON AIR FORCE BASE, OH 45433-7734

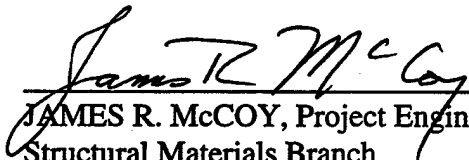
DTIC QUALITY INSPECTED 4

## NOTICE


When government drawings, specifications, or other data are used for any purpose other than in connection with a definitely Government-related procurement, the United States Government incurs no responsibility or any obligation whatsoever. The fact that the government may have formulated or in any way supplied the said drawings, specifications, or other data, is not to be regarded by implication, or otherwise in any manner construed, as licensing the holder, or any other person or corporation; or as conveying any rights or permission to manufacture, use, or sell any patented invention that may be related thereto.

This report is releasable to the National Technical Information Service (NTIS). At NTIS, it will be available to the general public, including foreign nations.


This technical report has been reviewed and is approved for publication.



JAMES R. McCOY, Project Engineer  
Structural Materials Branch  
Nonmetallic Materials Division



L. SCOTT THEIBERT, Chief  
Structural Materials Branch  
Nonmetallic Materials Division



ROGER D. GRISWOLD, Assistant Chief  
Nonmetallic Materials Division  
Materials Directorate

If your address has changed, if you wish to be removed from our mailing list, or if the addressee is no longer employed by your organization, please notify AFRL/MLBC, Bldg 654, 2941 P St, Ste 1, Wright-Patterson AFB OH 45433-7750 to help us maintain a current mailing list.

Copies of this report should not be returned unless return is required by security considerations, contractual obligations, or notice on a specific document.

REPORT DOCUMENTATION PAGE			Form Approved OMB No. 0704-0188	
<small>Public reporting burden for this collection of information is estimated to average 1 hour per response, including the time for reviewing instructions, searching existing data sources, gathering and maintaining the data needed, and completing and reviewing the collection of information. Send comments regarding this burden estimate or any other aspect of this collection of information, including suggestions for reducing this burden, to Washington Headquarters Services, Directorate for Information Operations and Reports, 1215 Jefferson Davis Highway, Suite 1204, Arlington, VA 22202-4302, and to the Office of Management and Budget, Paperwork Reduction Project (0704-0188), Washington, DC 20503.</small>				
1. AGENCY USE ONLY (Leave blank)		2. REPORT DATE August 1997	3. REPORT TYPE AND DATES COVERED Final Report - 9/15/95 - 6/2/97	
4. TITLE AND SUBTITLE MECHANICS OF BRITTLE-MATRIX COMPOSITES			5. FUNDING NUMBERS F33615-95-D-5029 PE 62102F PR 4347 TA 34 WU 10	
6. AUTHOR(S) Ran Y. Kim				
7. PERFORMING ORGANIZATION NAME(S) AND ADDRESS(ES) University of Dayton Research Institute 300 College Park Avenue Dayton, OH 45469-0168			8. PERFORMING ORGANIZATION REPORT NUMBER  UDR-TR-97-127	
9. SPONSORING/MONITORING AGENCY NAME(S) AND ADDRESS(ES) Materials Directorate Wright Laboratory Air Force Materiel Command Wright-Patterson AFB OH 45433-7734 POC: James R. McCoy, WL/MLBC, 937/255-9063			10. SPONSORING/MONITORING AGENCY REPORT NUMBER  WL-TR-97-4107	
11. SUPPLEMENTARY NOTES				
12a. DISTRIBUTION / AVAILABILITY STATEMENT  Approved for public release, distribution unlimited.			12b. DISTRIBUTION CODE	
13. ABSTRACT (Maximum 200 words)  Model brittle matrix composites (SiC fibers and borosilicate glass) demonstrated that good matrix cracking stress is achievable only when a good matrix interfacial bond exists. Improvement in this matrix cracking stress can be seen with increasing fiber volume and lowered radial residual compressive stress. The ability to measure the fiber-matrix normal interfacial strength in a composite was demonstrated using a model system in a cruciform sample geometry. An analytical model of ceramic composites based on observed damage progression was developed based on simultaneous stress application and microscopic observations. The damage state of the ceramic composite was successfully incorporated into the model to generate changes in the mechanical behavior. The measurement of coating modulus in BMCs was demonstrated using a microindenter technique.				
14. SUBJECT TERMS Brittle matrix composite, ceramic matrix composite, cruciform specimen, damage modes, debonding, fiber coating, microcracking, microindenter, micromechanics, model composite, modulus, normal interfacial strength, residual stress			15. NUMBER OF PAGES 57	
			16. PRICE CODE	
17. SECURITY CLASSIFICATION OF REPORT Unclassified	18. SECURITY CLASSIFICATION OF THIS PAGE Unclassified	19. SECURITY CLASSIFICATION OF ABSTRACT Unclassified	20. LIMITATION OF ABSTRACT SAR	

## CONTENTS

Section		Page
1	<b>CRACK INITIATION IN BRITTLE-MATRIX COMPOSITES</b>	<b>1</b>
	1.1 EXPERIMENTAL PROCEDURE	1
	1.2 EXPERIMENTAL OBSERVATIONS	4
2	<b>NORMAL STRENGTH IN MODEL UNIDIRECTIONAL COMPOSITES</b>	<b>14</b>
	2.1 EXPERIMENT	14
	2.2 RESULTS	17
	2.3 NUMERICAL ANALYSIS	19
	2.4 CHARACTERISTIC FAILURE DISTANCES FROM THE STRAIGHT-SIDED SPECIMENS WITH EXPOSED AND EMBEDDED FIBERS	22
	2.5 CONCLUSIONS	25
3	<b>DAMAGE MODES IN MULTIDIRECTIONAL CERAMIC-MATRIX COMPOSITES</b>	<b>26</b>
	3.1 EXPERIMENT	26
	3.2 ANALYTICAL BACKGROUND	27
	3.3 RESULTS	29
	3.3.1 Elastic Properties	29
	3.3.2 Damage Progression	30
	3.3.3 Stress-Strain Behavior	32
	3.4 SUMMARY	34
4	<b>MEASUREMENT OF ELASTIC MODULI OF FIBER COATINGS</b>	<b>35</b>
	4.1 EXPERIMENT	35
	4.2 RESULTS	36
5	<b>CONCLUSIONS AND RECOMMENDATIONS</b>	<b>41</b>
	5.1 CRACK INITIATION IN BRITTLE-MATRIX COMPOSITES	41
	5.2 NORMAL STRENGTH IN MODEL UNIDIRECTIONAL COMPOSITES	41

## **CONTENTS (Concluded)**

<b>Section</b>		<b>Page</b>
	5.3 DAMAGE MODES IN MULTIDIRECTIONAL CERAMIC-MATRIX COMPOSITES	42
	5.4 MEASUREMENT OF ELASTIC MODULI OF FIBER COATINGS	42
<b>6</b>	<b>PUBLICATIONS &amp; PRESENTATIONS</b>	<b>44</b>
<b>7</b>	<b>REFERENCES</b>	<b>45</b>

## FIGURES

Figure		Page
1	Typical Cross Section of a Borosilicate Glass Matrix (7040 Glass) Containing 16 vol% Sigma 1240 Fibers (Bar = 200 $\mu\text{m}$ )	3
2	Examples of Full- and Half-Cell Cracks in Borosilicate Glass-Matrix Composites: (a) Sigma 1240 and (b) SCS-6 (Bar = 200 $\mu\text{m}$ )	5
3	Edge of a 7040-Glass-Matrix Composite Containing Six Layers (35 vol%) of Sigma 1240 Fibers at (a) 101 MPa and (b) 112 MPa (Bar = 200 $\mu\text{m}$ )	6
4	The Number of New Cracks for Composite Specimens of F- and 7040-Glass Containing Comparable Fiber Volume Fractions	8
5	Stress-Strain Plots and Acoustic Emission Results for the Continuous Loading of Similar Specimens to those shown in Figures 4a and 4b	9
6	Semiempirical Model Predictions for a Continuous Interface and Experimental Measurements of the Composite Stress when Matrix Cracking Occurs versus Fiber Volume Fraction for (a) Sigma 1240 and (b) SCS-6 Fibers	12
7	Straight-Sided Specimen with Fiber Ends Exposed	15
8	Straight-Sided Specimen with Fiber Ends Embedded	15
9	Cruciform (or Cross-Shaped) Specimen	16
10	Photomicrographs of Aluminum Rod Specimen Showing Front and Back Views at the First Occurrence of Acoustic Emission on the Stress-Strain Curve (10a and 10b) and at Failure (10c and 10d), respectively	18
11	Photomicrograph of Failure Surface of Straight-Sided Specimens with Ends Embedded	20
12	Photomicrograph of Failure Surface of Cruciform (or Cross-Shaped) Specimens	20
13	Variation of Radial Stress with Normalized Distance from Center of the Specimen Along the Length of the Aluminum Rod	21

## FIGURES (Concluded)

Figure		Page
14	Variation of Transverse Strain with Normalized Distance from Center of the Specimen Along the Length of the Aluminum Rod	23
15	Photomicrograph Showing Partial Debonding of Fiber Matrix Interface and Extending into Matrix	30
16	Photomicrographs Showing Damage Progression for a $[0/90]_{3S}$ Laminate Specimen	31
17	Stress-Strain Relation for the $[0/90]_{3S}$ Laminate at Room Temperature	33
18	Experimentally-Measured Major Poisson's Ratio as a Function of Applied Stress for $[0/90]_{3S}$ Laminate at Room Temperature	33
19	Typical Load-Displacement Curve from a DSI Test	36
20	Micrograph Showing a Series of Indentations on the $90^\circ$ Surface	37
21	Load vs. Displacement on the $90^\circ$ Surface: Applied Load = 10 mN (a) Fiber; (b) c-Layer; (c) $TiB_2$ -Layer; (d) Matrix	38

## TABLES

Table		Page
1	Material Properties	3
2	Applied Stress at Debond Initiation for Model Composites	18
3	Predicted Bond Strength from Straight-Sided Specimen	24
4	Constituent Properties	28
5	Elastic Properties of Unidirectional Laminate	29
6	Elastic Properties of $[0/90]_{3S}$ Laminate	29
7	Summary of Test Results	37





## EXECUTIVE SUMMARY

Crack initiation in brittle matrix composites was investigated using model composites. Regular arrays of both  $\text{TiB}_2$ -coated and carbon-coated SiC fibers in borosilicate glass matrices were prepared. Fiber volumes and the thermal expansion mismatch between fiber and matrix were varied systematically. The  $\text{TiB}_2$  coating represented a strong interface and the carbon coating a weak interface between the fibers and the glass matrix. Test specimens were loaded in tension and monitored by acoustic emission for cracking with the number of cracks also quantified using optical microscopy.

With a strong interfacial bond, the level of matrix cracking stress increases with fiber fraction and decreases as the initial radial stress gets more compressive, both cases in agreement with prediction. When the initial radial stress is tensile, the theory overestimates the matrix cracking stresses. When poor interfacial bonding exists, the matrix cracking stress was found to be at the lower bound for a slipping interface even when the initial matrix stress is compressive.

A seldom-addressed area of composite mechanics, the fiber-matrix normal strength was examined. Unlike interfacial shear, the normal strength is very difficult to measure since free edges produce very strong singularities in stress. Samples with fiber ends embedded in the matrix and cruciform samples were examined. The latter, cross-shaped samples, were successful in forcing high normal stress levels at the fiber-matrix interface away from the free edges. The stresses measured on a model system (aluminum-epoxy) using the cruciform geometry matched theoretical predictions very well. This specimen geometry appears to be capable of generating true transverse properties of the fiber-matrix interface.

The damage modes in ceramic matrix composites were categorized by observing damage *in situ* under load. A silicon-carbide fiber glass-ceramic matrix composite with cross-ply reinforcement was placed under load and the types and extent of damage was observed by optical microscopy. The initial damage appears as fiber-matrix debonding and matrix cracking occur in the 90° plies. This damage continues until transverse cracks span all the 90° plies and then similar debonding and cracking begin in the 0° plies. Fiber-matrix debonding, matrix cracking, fiber breaks, and longitudinal splitting were identified and quantified as a function of uniaxial loading. Analytical predictions of the modulus and Poisson's ratio were then made based on those observations and idealized damage states corresponding to the observed states. The analytical models developed correlated very well with the observed mechanical behavior.

Another property of brittle matrix composites explored in this research was the measurement of elastic moduli of fiber coatings. The TiB<sub>2</sub>-coated and carbon-coated SiC fibers in borosilicate glasses above were examined using a microindenter. This well-established method using load-displacement curves during indentation has been used to measure the elastic moduli of fibers and matrices of composites. This technique was now applied to the coating layer between fiber and matrix. The values obtained for the fiber and matrix compare well to other researchers and are load independent and only slightly dependent on the indenter face angle. The low-cut angle values obtained on the coatings were very close to literature values but the high-cut angle was substantially higher. The high-cut angle indenter values may be erroneous due to the surrounding materials also being measured during the test. Additional work is underway to confirm this hypothesis.

## FOREWORD

This report was prepared by the University of Dayton Research Institute under Air Force Contract No. F33615-95-D-5029, Delivery Order No. 0002. The work was funded by the Air Force Office of Scientific Research and administered by the Nonmetallic Materials Division of the Materials Directorate, Wright Laboratory, Air Force Materiel Command, with Dr. James R. McCoy (WL/MLBC) as Project Engineer.

The author expresses his sincere appreciation to Dr. N. J. Pagano, WL/MLBM, and Dr. G. P. Tandon, AdTech Systems Research, for their support in conducting the numerical studies required for this work; R. Dutton, WL/MLLM, for supplying experimental composites for the tests conducted; R. Trejo, UDRI, for the mechanical characterization of composites and image analysis to detect damage; W. Ragland, UDRI, and J. Schuck, SOCHE, for fabricating model composite specimens; and Dr. A. Voevodin, SRL, for performing nanoindentation tests to determine the elastic properties of fiber coatings.

This report was submitted in August 1997 and covers work conducted from 15 Sep 1995 through 2 June 1997.

## 1. CRACK INITIATION IN BRITTLE-MATRIX COMPOSITES

The initiation of matrix microcracking was investigated in unidirectional glass-matrix composites having controlled fiber spacing. Observations were taken from composites consisting of regular arrays of  $\text{TiB}_2$ -coated Sigma 1240 and carbon-coated SCS-6 monofilament SiC fibers in a series of borosilicate glasses. The thermal expansion mismatch between the fibers and glass-matrix was varied such that the resulting radial stresses after processing ranged from tensile to compressive. The glass strongly bonds to the  $\text{TiB}_2$ -coated Sigma 1240 fiber but weakly bonds to the carbon coating of the SCS-6 fiber, allowing the investigation of the effects of bonding at the fiber/matrix interface. The observed crack initiation stresses of the various composites are compared to predictions based on a previously developed semiempirical model [1,2] and used to study the influence of the volume fraction of fibers, residual stress state, and interface strength.

### 1.1 EXPERIMENTAL PROCEDURE

The composites were fabricated from three borosilicate glasses with differing thermal expansion coefficients such that the resulting residual radial thermal stresses after processing varied from tensile to compressive. In addition two fibers were utilized: a 102- $\mu\text{m}$ -diameter Sigma 1240 fiber with an outer 0.5- $\mu\text{m}$ -thick  $\text{TiB}_2$  coating over an inner 1.5- $\mu\text{m}$ -thick carbon coating and a 142- $\mu\text{m}$ -diameter SCS-6 fiber with two 1.5- $\mu\text{m}$ -thick carbon coatings. The borosilicate glass strongly bonds to the outer  $\text{TiB}_2$  coating of the Sigma 1240 fiber but weakly bonds to the outer carbon coating of the SCS-6 fiber. This allowed an investigation of the effects of bonding at the fiber/matrix interface on the initiation of matrix cracking. Detailed calculations based on measured [3] elastic properties of these coatings for an uncracked matrix show that these stresses are insensitive to the elastic moduli of the coatings. Hence the coatings have been ignored.

Details of the sample fabrication are given in Reference [4] and are summarized below. The glass powders (average diameter of  $\sim 8 \mu\text{m}$ ) with varying  $\text{K}_2\text{O}/\text{B}_2\text{O}_3$  ratios were tape-cast into green tapes with a relative density of  $\sim 50$  percent. The glass compositions were graded in order to vary the thermal expansion coefficient of the glass. The green tapes were cut into coupons  $100 \times 100\text{-mm}$  square and laminated onto fiber mats with a regular fiber spacing of either 27 or 48 fibers per cm. The volume fraction of fibers in the composites was varied by altering the thickness of the green tape and utilizing the two different fiber spacings. After lamination the composites were vacuum sintered at  $710^\circ\text{C}$  for one hour, after which the tube furnace was backfilled with Argon for 20 minutes. The samples were then hot isostatically pressed at  $650^\circ\text{C}$  for 30 minutes with an applied pressure of 35 MPa to remove residual porosity to typically  $< 2$  percent. The resulting samples were approximately 10 cm long by 2 cm wide with a thickness of 0.2 cm. Figure 1 shows a typical sample cross section of a Sigma 1240 fiber composite and illustrates the regularity of the fiber spacing.

Prior to testing, the free edges of the specimens were polished with diamond paste in order to enhance microscopic imaging for crack detection. The upper and lower surfaces were coated with a thin layer of epoxy to reduce the incidence of surface damage during handling and to attempt a more realistic simulation of interior matrix cracking. The testing was performed in an MTS testing machine at a loading rate of 0.25 mm/min. Axial and transverse strains were measured using strain gages. The volume fraction of fibers in each specimen was determined from the measured elastic modulus of the composite using the rule-of-mixtures and the moduli of the respective fibers and matrices as determined by separate tests. These compared well with measurements taken from optical micrographs of selected sample cross sections. The properties of the composite constituents are presented in Table 1.

Acoustic emission techniques were employed for the detection of initial matrix cracking. After the detection of cracking by acoustic emission, the edges of the specimen were coated with fluorescent dye while the sample remained under load. The specimen was then removed from the

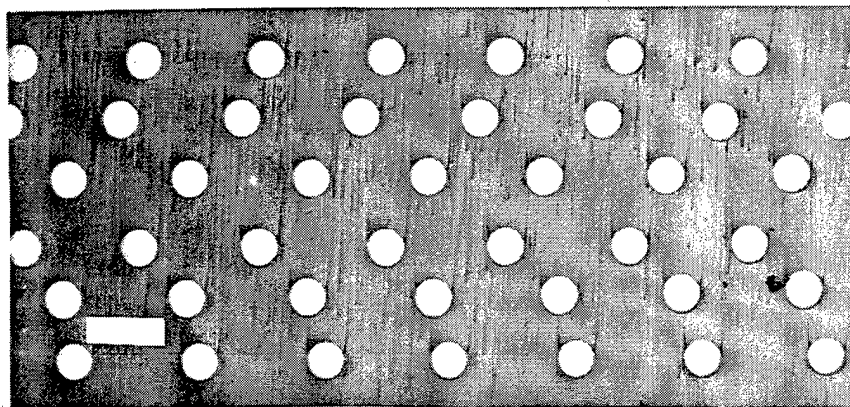


Figure 1. Typical Cross Section of a Borosilicate Glass Matrix (7040 Glass) Containing 16 vol% Sigma 1240 Fibers (Bar = 200  $\mu\text{m}$ ).

TABLE 1  
MATERIAL PROPERTIES

	Glass			Fibers	
	7040	F	E	Sigma 1240	SCS-6
E (GPa)	50	58	58	325	390
$\nu$	0.20	0.20	0.20	0.20	0.20
$\alpha$ ( $\times 10^{-6}/^{\circ}\text{C}$ )	5.40 <sup>a</sup>	4.25 <sup>a</sup>	3.95 <sup>a</sup>	4.23 <sup>b</sup>	4.23 <sup>b</sup>
$K_{IC}$ (MPa - $\sqrt{\text{m}}$ )	0.77	0.77 <sup>c</sup>	0.77	--	--

Note: Data measured at WL/ML unless otherwise indicated.

a - Corning Glass Works, Corning, NY

b -  $\beta$ -SiC (0-500°C), Southern Research Institute, Birmingham, AL

c - Assumed same as 7040 and E-glasses

testing machine, and the location and spacing of matrix cracks determined by optical microscopy. Typical full-cell cracks, characterized by a crack surrounding a single fiber, are shown in Figures 2a and 2b. The specimen was then mounted in the testing machine and the load incremented, until acoustic emission indicated that further matrix cracking had occurred. The edges of the specimen were again coated with fluorescent dye and the sample removed from the test machine and the crack pattern examined. This procedure continued in a stepwise manner until the sample failed.

## 1.2 EXPERIMENTAL OBSERVATIONS

Clearly, unless one can define the distribution of inherent matrix flaws prior to cracking, the matrix cracking stress must be treated as a statistical process. Thus, the first crack to form is not a representative measure of the matrix strength. Rather, by considering a number of cracks spaced such that they do not interact with each other, an average value of the matrix cracking stress can be computed. It is in this sense that progressive microcracking [1,2] represents a characteristic value of the matrix cracking stress. Thus, the composite cracking stress,  $\sigma_c$ , the stress in the composite at which matrix cracking initiates, was determined from a plot of the number of new cracks versus load. New cracks were defined as cracks that were not extensions of cracks from previous loadings and which were separated from earlier cracks by an axial distance of at least 150  $\mu\text{m}$ . An axial distance of 150  $\mu\text{m}$  was selected based on calculations of the stress [5,6] in the matrix as a function of the axial distance from the crack plane assuming that no debonding has occurred. It is reasonable to assume that there is no interaction between cracks separated by an axial distance of 150  $\mu\text{m}$  or more. Thus, each new crack obviously defines an initiation event.

The counting technique is illustrated by Figures 3a and 3b which are photomicrographs of the edge of a composite specimen containing 35 vol% Sigma fibers in a 7040-glass matrix after loading to 109 MPa and 125 MPa, respectively. The matrix cracks in Figure 3(a) initiated and some of these cracks appear to have been stopped by the fibers. This crack morphology, i.e.,



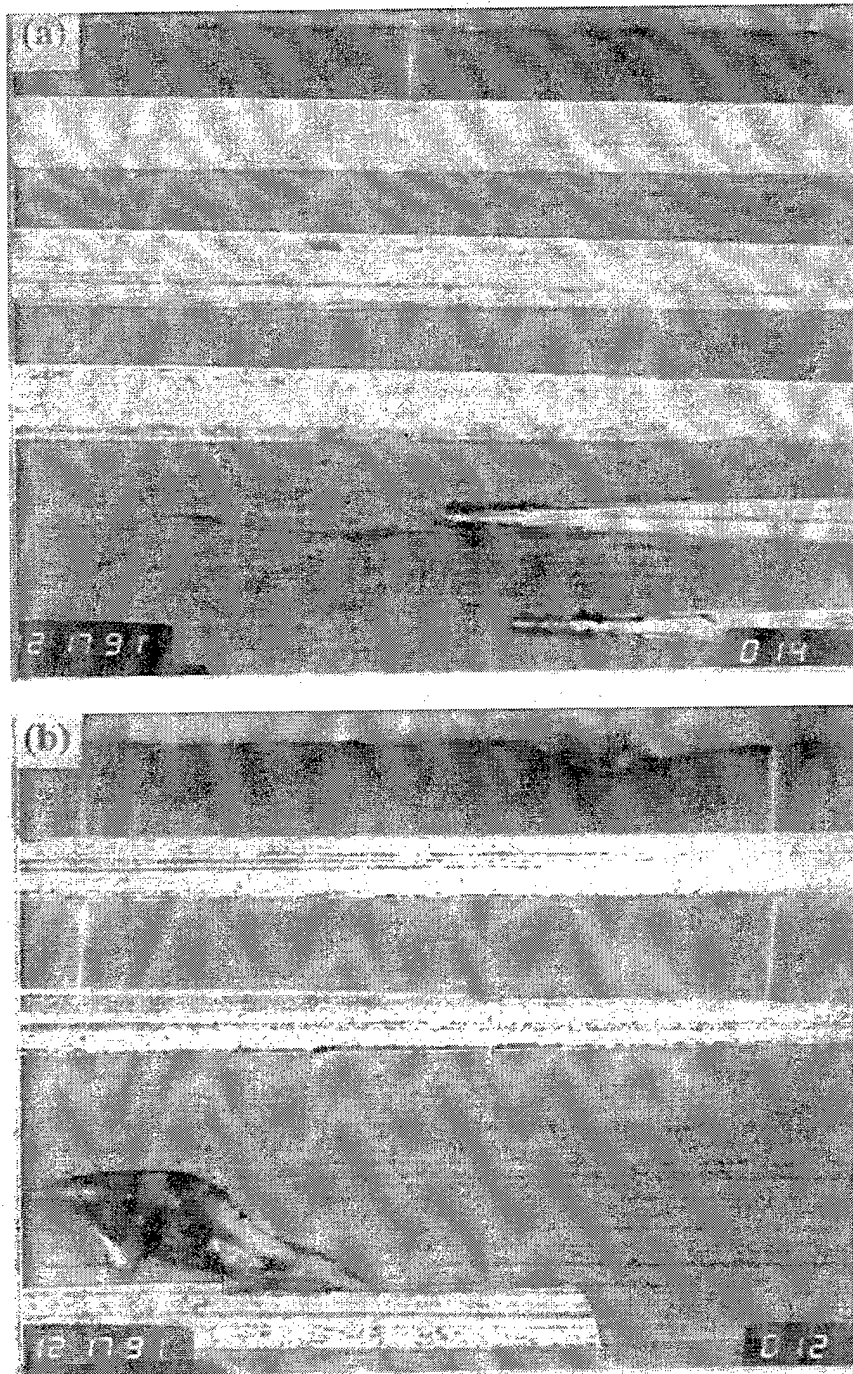


Figure 2. Examples of Full- and Half-Cell Cracks in Borosilicate Glass-Matrix Composites: (a) Sigma 1240 and (b) SCS-6 (Bar = 200  $\mu\text{m}$ ). Full-cell cracks are characterized by a crack which bridges a single fiber but is arrested by adjacent fibers; half-cell cracks are confined between two fibers.

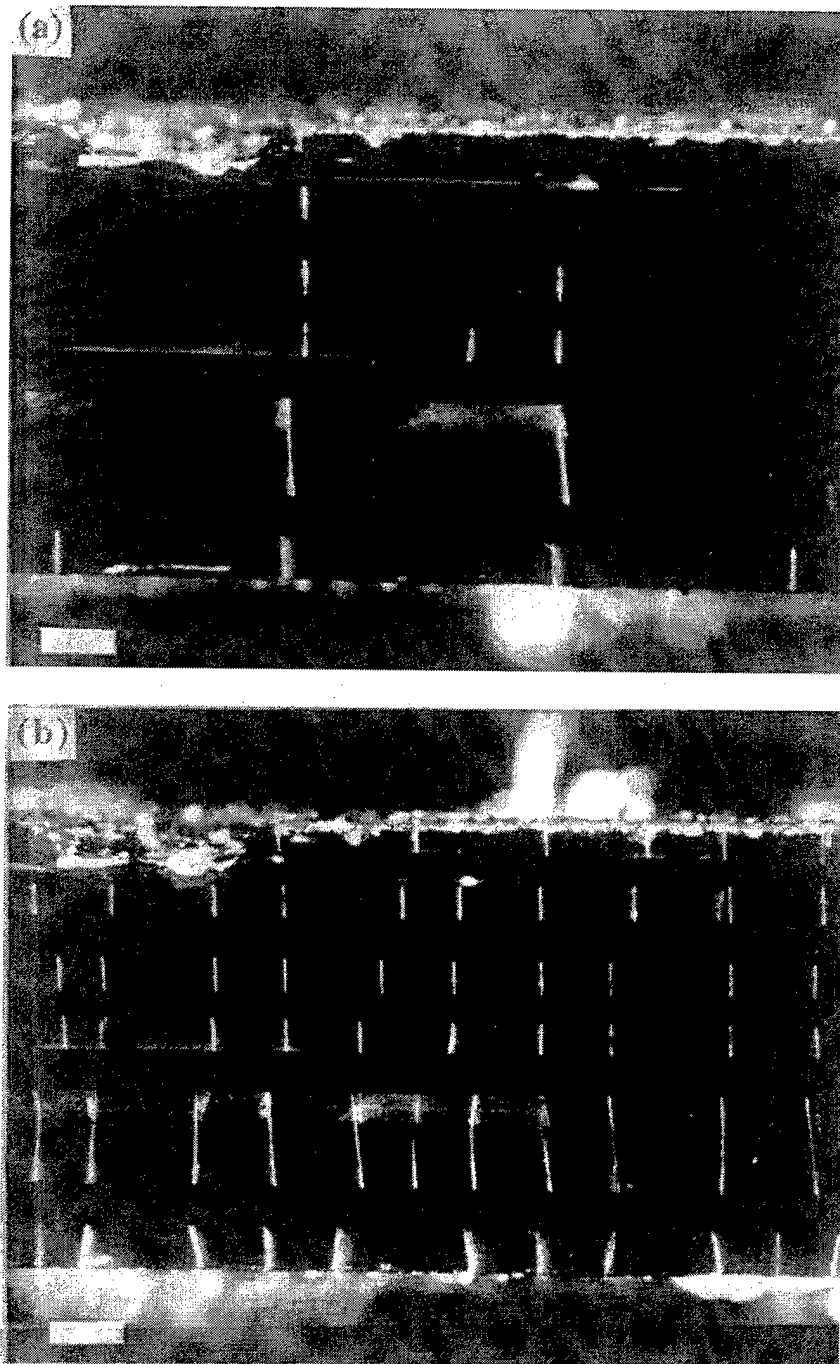


Figure 3. Edge of a 7040-Glass-Matrix Composite Containing Six Layers (35 vol%) of Sigma 1240 fibers at (a) 109 MPa and (b) 125 MPa (Bar = 200  $\mu\text{m}$ ).

localized fiber bridging of widely spaced cracks, is characteristic of that seen in other brittle-matrix composite (BMC) systems [1,2]. Upon subsequent loading (Figure 3b) some of the cracks present in Figure 3a have propagated across the sample, and new cracks have formed above and below the initial ones. Based on the criteria described above, there are five new cracks in Figure 3a and seven in Figure 3b. Importantly, although matrix cracks had formed, the stress-strain curves associated with Figures 3a and 3b showed no detectable loss of stiffness.

The determination of the composite cracking stress from the population of new cracks is illustrated in Figure 4, a plot of the number of new cracks versus applied stress for two composite specimens containing comparable fiber volume fractions: (a) an F-glass with 28 vol% and (b) a 7040-glass with 30 vol% Sigma 1240 fibers. Also shown are the respective precrack tensile axial stresses,  $\sigma^T$ , in the matrix due to the thermal expansion coefficient mismatch between the SiC fibers and the glasses. For comparison purposes the number of new cracks at each load level has been normalized by the total number of new cracks that were counted in each specimen (102 and 515, respectively). In both specimens the number of new cracks increases sharply to a peak and then falls off. The composite stress at which the steplike increase in the number of new cracks occurs is defined as  $\sigma_c$ . It is important to note that the model assumes an interior crack, while only surface cracks can be observed. While the specimen was prepared in such a way as to approximate interior crack formation (e.g., coating the upper and lower surfaces with a thin layer of epoxy to reduce the incidence of surface damage), the simulation is not perfect. The decay in the number of new cracks after reaching a peak value does not imply that the matrix has become saturated with cracks, only that subsequent cracks are either extensions of previous cracks or occur at an axial distance less than 150  $\mu\text{m}$  from existing cracks. Typically, crack saturation occurred a few loadings prior to sample failure which were, in general, at applied stresses greater than 250 MPa, i.e., well above the composite cracking stress. The results shown in Figure 4 indicate that the composite cracking stress is strongly affected by the thermal loading of the matrix, which was calculated assuming a thermoelastic cooldown process. That is,

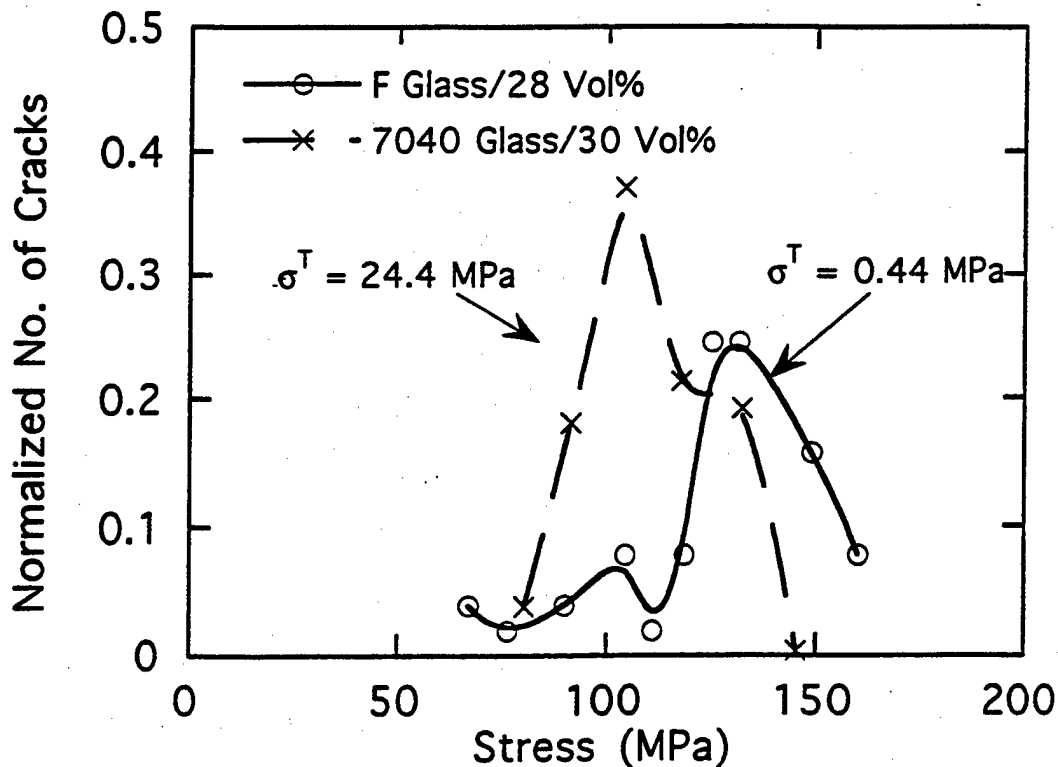
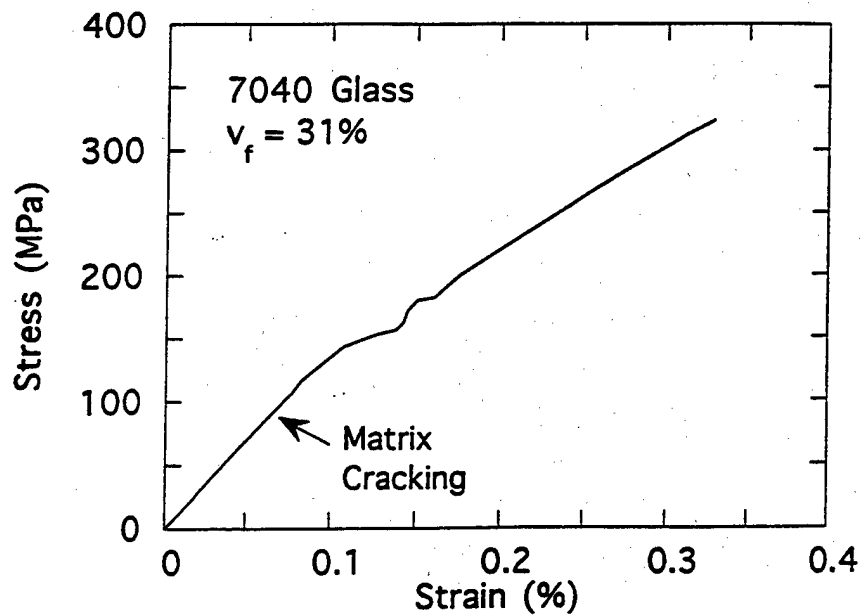


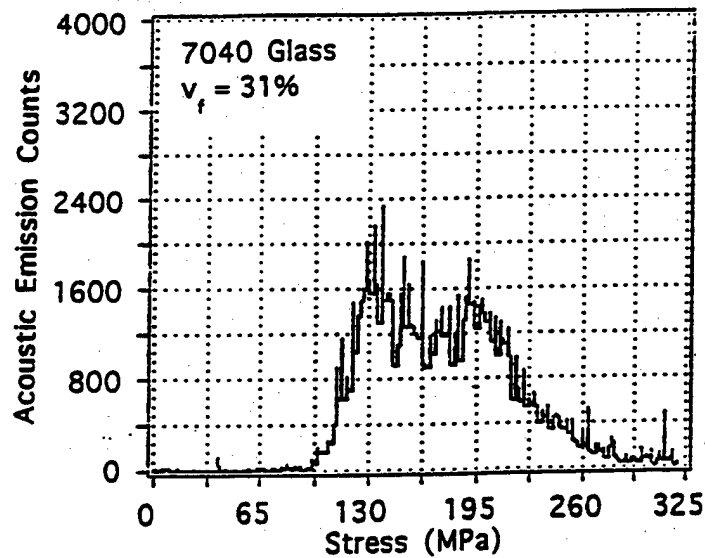
Figure 4. The Number of New Cracks for Composite Specimens of F- and 7040-Glass Containing Comparable Fiber Volume Fractions. The number of new cracks has been normalized by the total number of new cracks in each specimen. Also shown are the precrack tensile axial stresses,  $\sigma^T$ , in the matrix due to the thermal expansion mismatch between the fiber and the matrix.

the F-glass composite with a residual axial tensile stress in the matrix of 0.44 MPa has a  $\sigma_c$  that is ~30 MPa greater than the 7040-glass composite which has a residual axial stress of 24.4 MPa.

Figures 5a-d are the stress-strain plots and acoustic emission (AE) results for the continuous loading of similar specimens to those shown in Figure 4 (i.e. samples prepared from the same green laminate). The AE results shown in Figures 5b,d have a similar steplike increase in the number of AE events at a load corresponding to the  $\sigma_c$  determined from the incremental loadings shown in Figure 4. This increase occurs ~15 MPa below the onset of any deviation from linearity in the stress-strain curve. Similar behavior has been observed in other BMCs [7]. Indeed, the onset of nonlinearity in the stress-strain curve, typically associated with a large jump

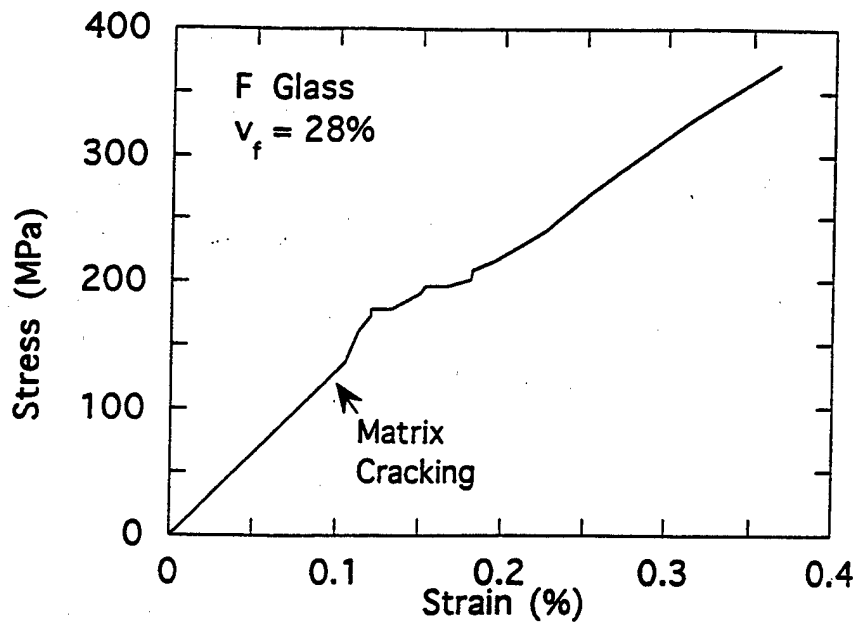


(a)

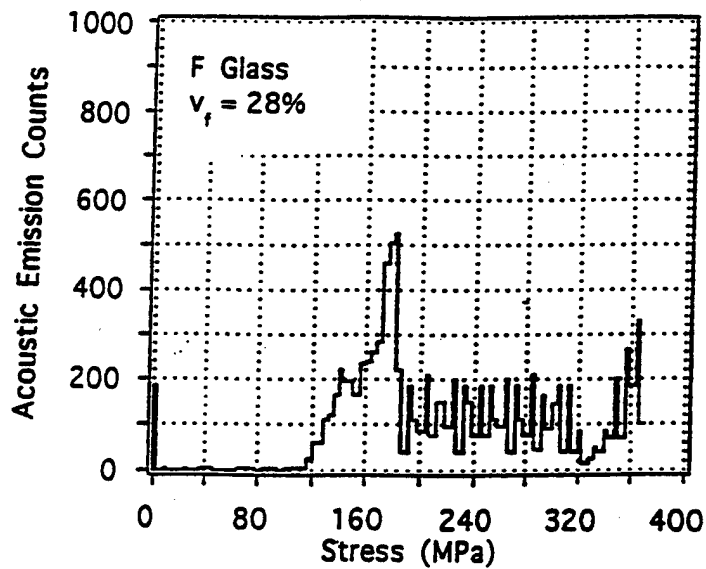


(b)

Figure 5. Stress-Strain Plots and Acoustic Emission Results for the Continuous Loading of Similar Specimens to those shown in Figures 4a and 4b. The composite stress at matrix cracking,  $\sigma_c$ , is ~15 MPa below the onset of nonlinearity in the stress-strain curve.



(c)



(d)

Figure 5. (Concluded). Stress-Strain Plots and Acoustic Emission Results for the Continuous Loading of Similar Specimens to those shown in Figures 4a and 4b. The composite stress at matrix cracking,  $\sigma_c$ , is  $\sim 15$  MPa below the onset of nonlinearity in the stress-strain curve.

in the number of acoustic emission events, correlated with the observation of broken fibers at the outer edge of the specimen.

Calculation of cracking stress  $\sigma_m$  was accomplished using the following expression [2]

$$2\sigma_m[(a+s)/\pi]^{1/2} = K_{IC} \quad (1)$$

where  $a$  is the fiber radius,  $s$  is the fiber spacing, and  $K_{IC}$  is fracture toughness. The fiber spacing associated with a given fiber volume fraction was calculated assuming the hexagonal array. The  $K_{IC}$  value of  $1.84 \text{ MPa } \sqrt{\text{m}}$  [2] was used. This model (Equation 1) predicts that the matrix cracking stress increases with decreasing values of  $s$  and  $a$ .

In order to compare with the experimental results, the composite stress ( $\sigma_c$ ) was calculated for the given  $\sigma_m$ . The model and experimental results are plotted in Figures 6a and 6b. Figure 6a (Sigma 1240 fiber) shows that the model with a continuous interface closely matches the experimental results for the 7040- and F-glass (i.e., precrack compressive  $\sigma_r$ ) but overestimates the E-glass (i.e., precrack tensile  $\sigma_r$ ) results. Figure 6b (SCS-6 fiber) shows that most of the experimental results are closer to the lower bound model prediction with a sliding frictionless interface than to any of the continuous interface model predictions. As noted before the borosilicate glasses do not strongly bond to the carbon coating of the SCS-6 fiber. Thus an explanation of the SCS-6 fiber composite results may be that the fiber/matrix interface is relatively weak, allowing interfacial slip to occur.

From the above results it can be concluded that there is a strong correlation between the analytical model, which depends only on measured properties, and the experimentally-measured composite cracking stress for composites with both a continuous interface (Sigma 1240 fibers) and a sliding frictionless interface (SCS-6 fibers). For composites containing Sigma 1240 fibers where  $\alpha_m > \alpha_f$ , the matrix cracking stress increases with fiber volume fraction but decreases as the magnitude of the tensile axial residual stress increases. Although the analytical model suggests that an axial compressive stress (i.e.  $\alpha_m > \alpha_f$ ) will act to increase the composite cracking stress, the experimentally-measured values were below those predicted by this model.

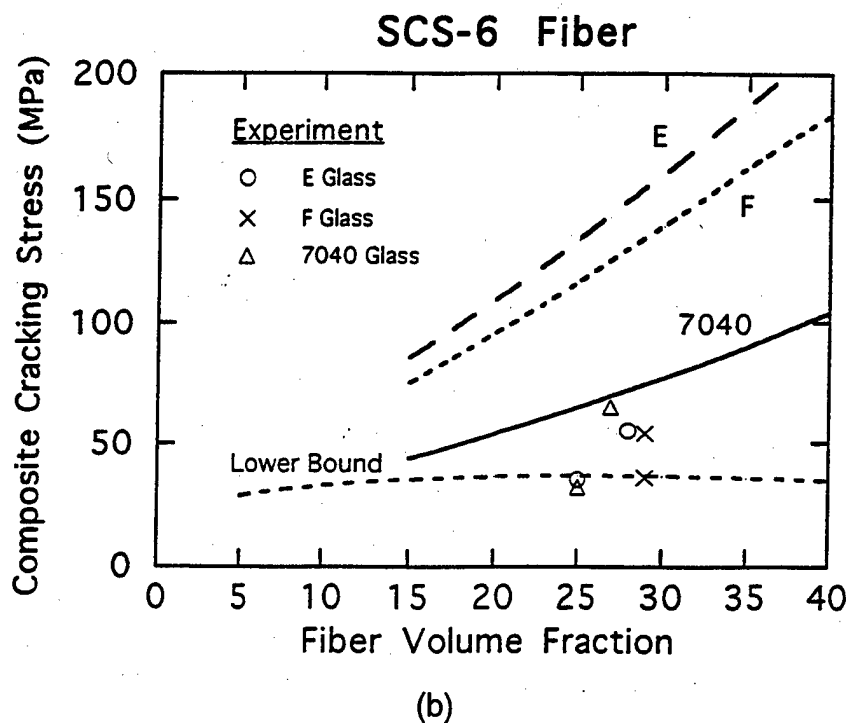
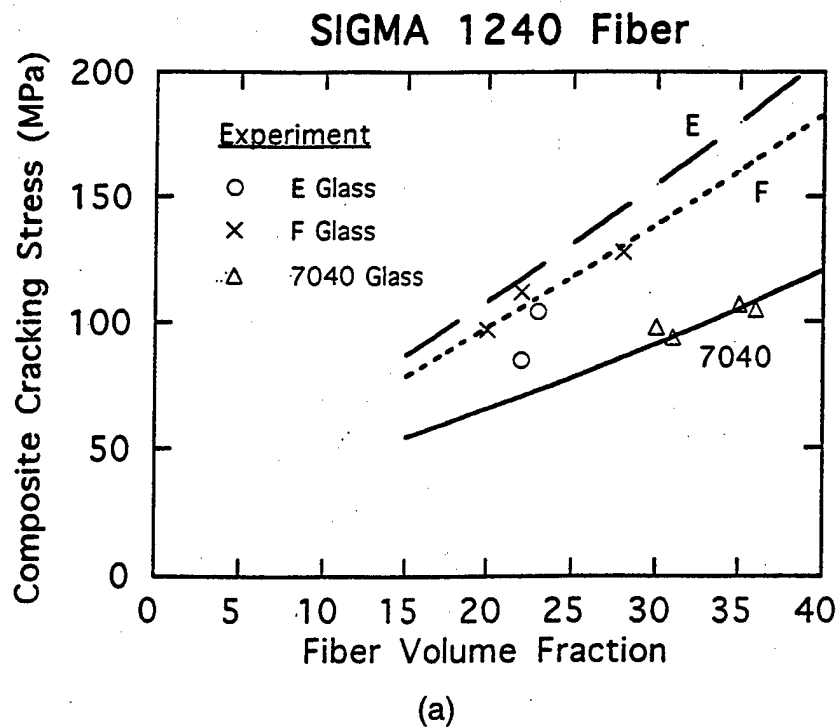


Figure 6. Semiempirical Model Predictions for a Continuous Interface and Experimental Measurements of the Composite Stress when Matrix Cracking Occurs versus Fiber Volume Fraction for (a) Sigma 1240 and (b) SCS-6 Fibers. Figure 6b includes model predictions for a lower bound representing a sliding frictionless interface.



Examination of the fracture surfaces of failed specimens revealed evidence which may represent partial debonding during processing which would reduce the composite cracking stress.

Comparing composites with weakly bonded interfaces (i.e., SCS-6 fibers) with strongly bonded interfaces (i.e., Sigma 1240 fibers), it was found that a strong interface enhances the matrix cracking stress, provided crack deflection occurs. In general these results provide further evidence of an increase in the matrix cracking stress level for composites with small-diameter, uniformly-spaced fibers.

## **2. NORMAL STRENGTH IN MODEL UNIDIRECTIONAL COMPOSITES**

Failure modes of fiber-reinforced composites are governed in part by the transfer of stress between fiber and matrix. This transfer occurs across the interface between the components; therefore, the properties of this interface will affect the properties of the composite. Unlike the interfacial shear strength, the measurement of the interfacial normal strength [8] has, to our knowledge, received limited attention. Therefore the present study is aimed at designing and evaluating some simple test methods for estimating the normal strength of the fiber-matrix interface.

Interfacial normal strength is commonly determined by testing straight-sided, single-fiber composite specimens (Figure 7) and interpreting debond initiation from the beginning of nonlinearity or first occurrence of acoustic emission on the stress-strain curve. In these straight-sided specimens, the free surface is a favored site for interface debonding because stresses are singular at that location. In order to remove the influence of the free surfaces from the test, two alternate geometries can be considered. The first design involves covering the ends of the fiber by embedding the fiber [9,10] completely inside the matrix (Figure 8), whereas the second design is of a composite sample in the shape of a cruciform or cross [11] with an extremely large width in the gage section (Figure 9). With the cross-shaped geometry, the central portion of the fiber/matrix interface is highly stressed under tensile loading, thereby forcing debond initiation and propagation in the center, away from the free edges.

### **2.1 EXPERIMENT**

Single-fiber composite tests are increasingly recognized as a most useful tool to study the mechanical/chemical interactions at the fiber-matrix interface region. Single-fiber specimens are easier to make compared to unidirectional composites, avoiding the difficulty of fiber alignment in unidirectional composites. Further, single-fiber composites help to focus on localized failure,

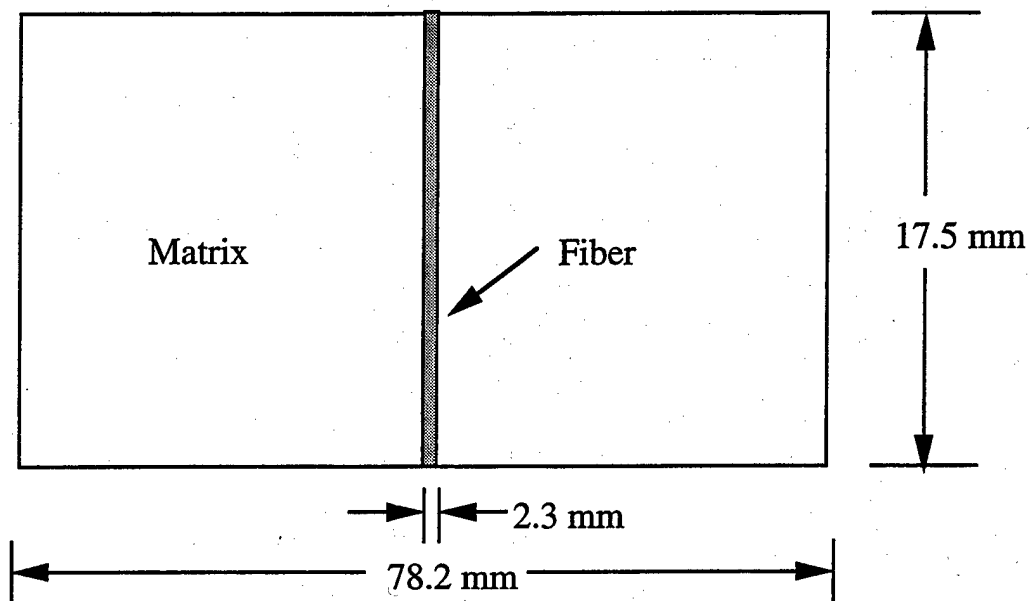


Figure 7. Straight-Sided Specimen with Fiber Ends Exposed.

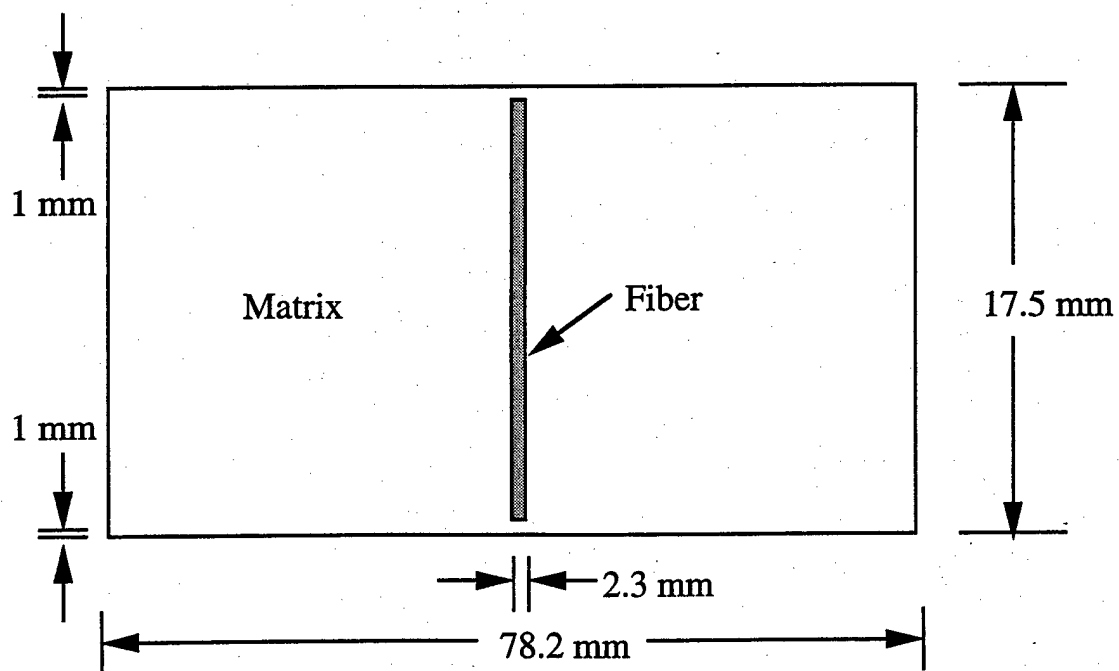


Figure 8. Straight-Sided Specimen with Fiber Ends Embedded.

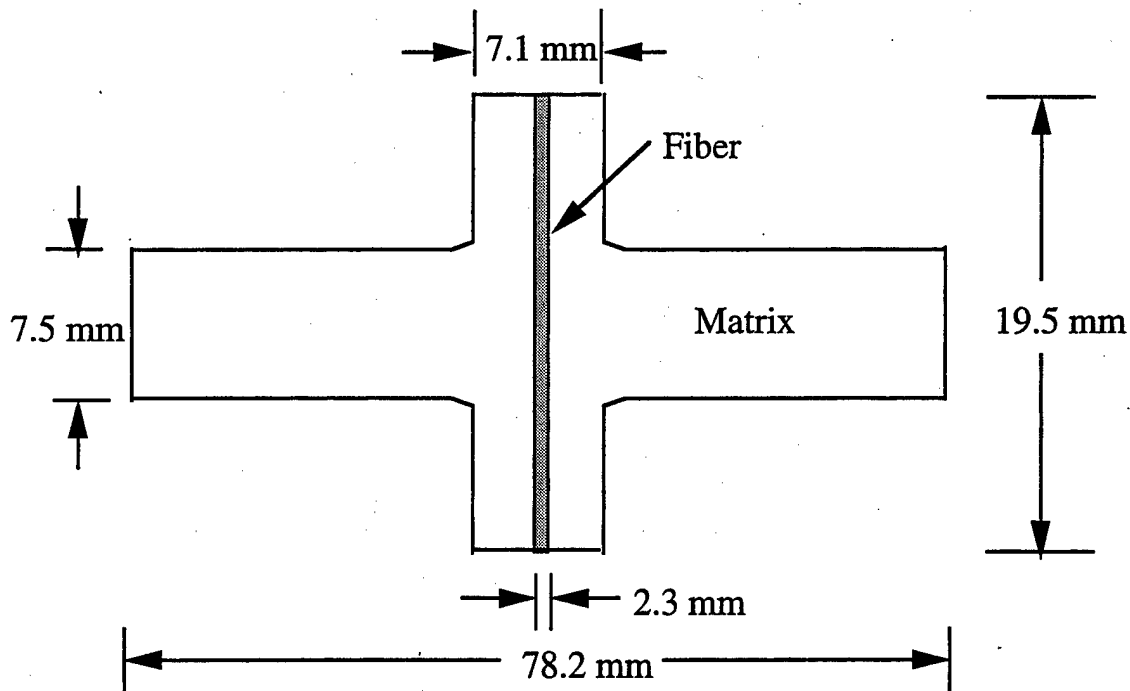


Figure 9. Cruciform (or Cross-Shaped) Specimen.

such as interface debonding, avoiding the distraction of randomness in failure and the neighboring effect of other fibers in unidirectional composites. In this work, model single-fiber composite specimens were made in the three geometrical configurations, namely: (a) straight-sided specimens with fiber ends exposed, (b) straight-sided specimens with fiber ends covered, and (c) cross-shaped design.

The composite specimens were cast in rectangular and cruciform-shaped silicone rubber molds for straight-sided and cross-shaped samples, respectively. The specimen cross-sectional dimensions are shown in Figures 7-9. The samples were 5.03 mm thick for all three geometries considered. The composite reinforcement consisted of aluminum rods, 2.34 mm in diameter, while the matrix was an epoxy resin (Epon 828 from Shell Chemical Co.) cured with a polyetheramine (Jeffamine D-230 from Texaco, Inc.) for three days at ambient temperature. The rod surfaces were merely cleaned with acetone which enabled the epoxy to strongly bond with the reinforcement. Rods of predetermined length were approximately positioned in the mold and epoxy resin cast around them. Curing at ambient temperature eliminated thermal residual

stresses which are otherwise induced from the mismatch in coefficients of thermal expansion of fiber and matrix.

The free edges of the straight-sided specimen with exposed fiber ends were progressively ground and then polished using successively smaller diameter alumina polishing powder (final size was 0.3 micrometer) in order to enhance the microscopic image for crack detection. The free edges of the cruciform specimen and straight-sided samples with embedded fiber ends were also polished after curing. Strain gages (gage length 3.2 mm) were then mounted on the flat surface in the center and along the edges of the specimen perpendicular to the fiber to monitor strain during loading. An acoustic emission transducer was also attached to the specimen to monitor failure events. For straight-sided samples with fiber ends exposed, the specimen was loaded to either a prescribed level slightly higher than the expected interface debonding level or up to the first occurrence of acoustic emission on the stress-strain curve. This load was held during application of a fluorescent penetrant to the polished surface, and then unloaded for microscopic examination to capture all failure events which occurred. Straight-sided samples with fiber ends embedded and cruciform-shaped specimens were also loaded in tension, under displacement control, to failure, and the fractured halves examined to identify the locus of failure.

## 2.2 RESULTS

The applied stress level at debond is listed in Table 2. The values listed in this table are the average of six specimens for each configuration considered.

Figures 10a and 10b are photomicrographs showing the front and back views of the straight-sided exposed fiber specimen at the first occurrence of acoustic emission on the stress-strain curve, respectively. The portion of the interface which was observed to be debonded under the microscope is indicated by arrows. Notice the symmetric nature of the debonded interface, with respect to the horizontal loading axis, observed both in front (Figure 10a) and back (Figure 10b) of the specimen. Subsequent loading resulted in the debond crack branching into the matrix

TABLE 2  
APPLIED STRESS AT DEBOND INITIATION FOR MODEL COMPOSITES

Model Single Fiber Specimen	Average Applied Stress at Debond Initiation, MPa	Standard Deviation (%)
Straight-Sided with Fiber Ends Exposed	8.3	14.1
Straight-Sided with Fiber Ends Embedded	12.3	4.6
Cruciform (Cross-Shaped)	19.5	6.7

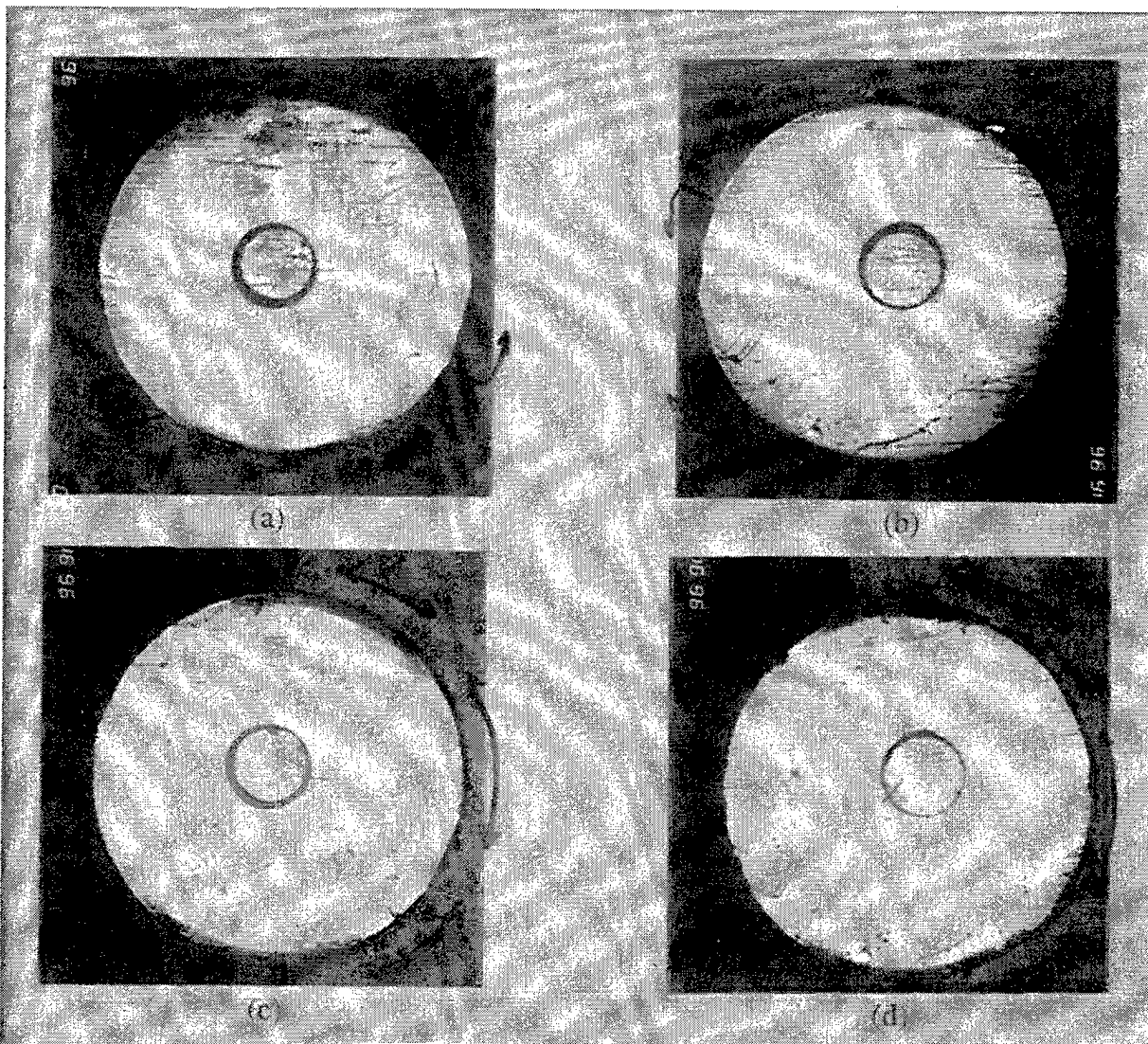


Figure 10. Photomicrographs of Aluminum Rod Specimen Showing Front and Back Views at the First Occurrence of Acoustic Emission on the Stress-Strain Curve (10a and 10b) and at Failure (10c and 10d), respectively.

leading to final failure as shown in the front and back of the specimen in Figures 10c and 10d, respectively. Figure 11 is a photomicrograph of the failure surfaces of a straight-sided specimen with fiber ends covered. It is seen that failure initiates at the fiber corner and propagates over some distance along the fiber length before branching into the matrix. However, for cruciform (or cross-shaped) specimens, it is observed that failure initiates in the center (region free of stress singularities) away from the fiber ends, as seen in the photomicrograph in Figure 12. The debond propagates for some distance along the length of the reinforcement before branching into the matrix.

### 2.3 NUMERICAL ANALYSIS

In this work model single-fiber composite specimens have been analyzed using 3-D finite element analysis employing the ANSYS code. The model was simplified by using symmetry planes so that only one-eighth of the total specimen was required to be modeled. These planes of symmetry were constrained by symmetry boundary conditions, whereas the outer surfaces were free to move in all directions. The aluminum reinforcement and the epoxy matrix were treated as three-dimensional, eight-node brick elements with the following elastic properties (handbook values).

Material	E(GPa)	$\nu$
Aluminum	72.4	0.32
Epoxy	2.9	0.35

Figure 13 shows the radial stress at the fiber-matrix interface in the loading direction as a function of distance along the length of the reinforcement for the three specimen geometries considered. Analysis reveals that the radial stress at the interface is the dominant stress component and is maximum in the loading direction. The local stresses are represented by the stress concentration factor (SCF), defined as the ratio of the local stress to the applied stress. The distance is normalized with respect to the radius of the aluminum rod. The SCF value is 1.2 in the center of the cruciform specimen and remains reasonably constant (within 10 percent) over

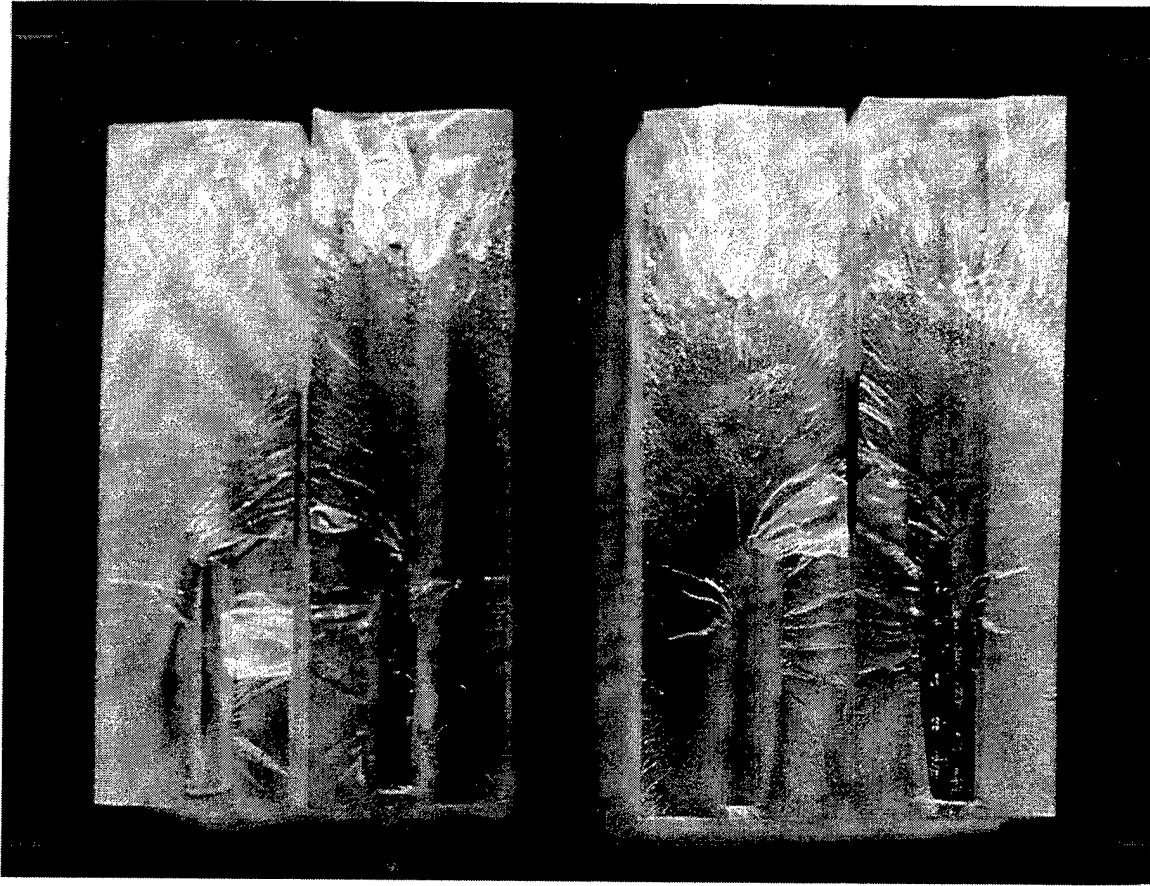


Figure 11. Photomicrograph of Failure Surface of Straight-Sided Specimens with Ends Embedded.

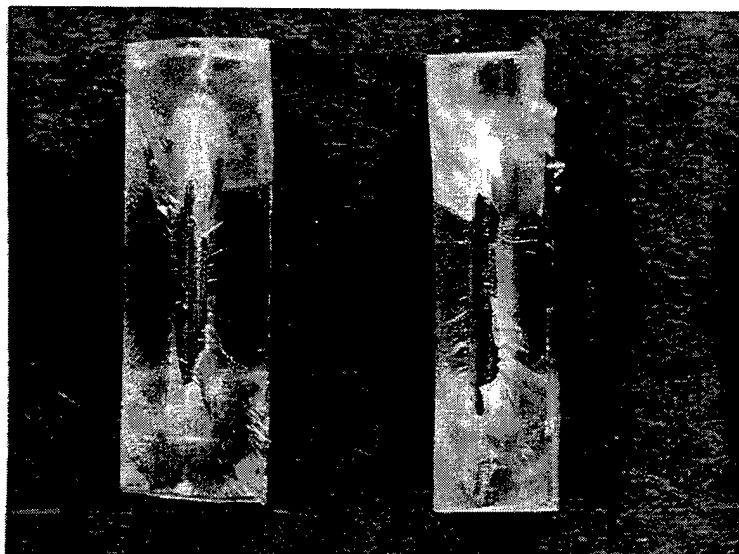


Figure 12. Photomicrograph of Failure Surface of Cruciform (or Cross-Shaped) Specimens.



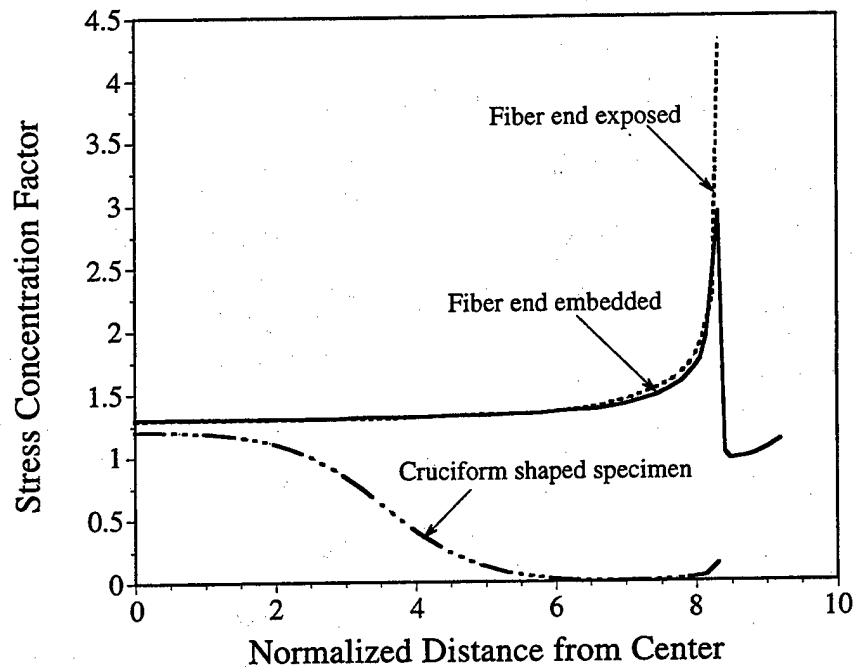


Figure 13. Variation of Radial Stress with Normalized Distance from Center of the Specimen Along the Length of the Aluminum Rod.

two-thirds of the loading region. The SCF gradually decreases at locations further away from the center of the specimen approaching zero value before increasing marginally near the free surface. For straight-sided samples the SCF at the center of the specimen is approximately 1.3 for both embedded and exposed fiber ends. However, as the free surface is approached for the exposed rod or the edge of the embedded rod is approached, a sharp increase in the SCF is observed, although the stresses in the latter are significantly lower than the former.

The results in the previous sections for the specimens tested indicated that only in the case of the cruciform specimen did interface failure occur far from the ends (where a factor of 1.2 is more appropriate due to partial loading of the wings), and that cracking initiated at the fiber corners in both the straight-sided and embedded fiber specimens. The likely explanation for this behavior is the high radial stresses that occur at the fiber corners for both the exposed-fiber and embedded-fiber specimens as seen in Figure 13. The lower far-field applied stress at debonding

for these specimens, compared with the cruciform geometry, is consistent with the local elevation of radial stress at the interface.

Figure 14 shows the transverse strain at the free surface of the cruciform specimen as a function of the distance along the length of the aluminum rod at locations which represent the positions of the strain gages in the experiments. The strain values have been normalized with respect to the applied stress level and measured matrix modulus. As seen in Figure 14, the experimentally-measured values of strain were within 10 percent of the calculated value at several locations along the length of the aluminum rod. Excellent match between strain calculations and measurements has also been obtained previously for metal-matrix composite cruciform-shaped specimens [12].

#### **2.4 CHARACTERISTIC FAILURE DISTANCES FROM THE STRAIGHT-SIDED SPECIMENS WITH EXPOSED AND EMBEDDED FIBERS**

The singular stress profiles for the straight-sided exposed-fiber and embedded-fiber specimens indicate that there are two ways any useful data can be obtained from such specimens. As an extreme case, the singular stress profile can be used to imply that a crack already exists at the fiber ends of the interface, so that the maximum load in the tensile test simply reflects the attainment of criticality based on the fracture toughness of the interface. The problem with this approach is that it requires some method of determining the initial crack length. The alternate approach is to assume that the failure of the interface is governed by a probability distribution, whereby failure occurs when area integrated probability of failure reaches a critical value. Therefore, even though stress can become infinite over an infinitesimal distance, the probability of failure will remain finite, being determined by the integrated probability of failure. In this study the focus is to determine a characteristic distance for the exposed and embedded-fiber specimens, so that the apparent strength of the interface from those specimens is equal to that from the cruciform specimen.

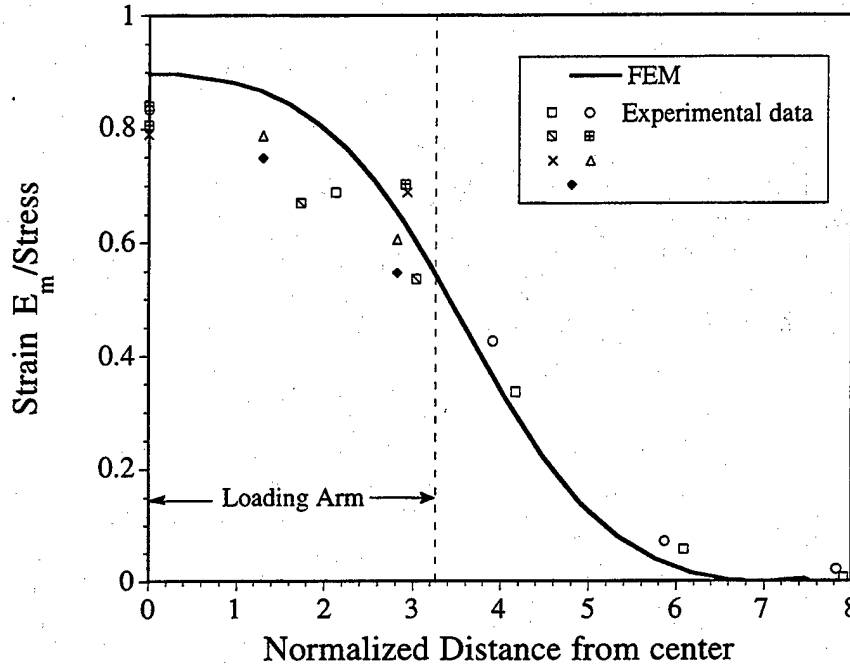


Figure 14. Variation of Transverse Strain with Normalized Distance from Center of the Specimen Along the Length of the Aluminum Rod.

To do this, we express the interface stress close to the fiber ends in the form [13]:

$$\sigma_{rr} / \sigma_a = k(r / R)^{-\lambda} \quad (2)$$

where we now identify  $r$  with the length of the fiber ( $z$ ) starting from the fiber end, and  $k$  and  $\lambda$  are the quantities determined from finite element analysis. Integrating the average stress concentration factor,  $SCF_{avg}$ , over a normalized distance,  $z_{avg}/R$  is then given by

$$SCF_{avg} = \frac{\sigma_{rr}^{avg}}{\sigma_a} = \frac{k}{(1-\lambda) \left( \frac{z_{avg}}{R} \right)^\lambda} \quad (3)$$

Note that the fitted parameters,  $\lambda$  and  $k$ , in Equations (2) and (3) vary with the averaging distance over which they are evaluated, as seen in Table 3. Moreover, the values of  $\lambda$  reported in Table 3 differ somewhat from the values obtained from asymptotic analysis (Table 2). The use of the fitted parameters, which vary with averaging distance, is justified in lieu of Equation (3)

TABLE 3  
PREDICTED BOND STRENGTH FROM STRAIGHT-SIDED SPECIMEN

Distance	Straight-Sided with Fiber Ends Exposed				Straight-Sided with Fiber Ends Embedded			
$\left(\frac{z_{avg}}{R}\right)$	$\lambda$	k	$\frac{\sigma_r^{avg}}{\sigma_a}$	Bond Strength, MPa*	$\lambda$	k	$\frac{\sigma_r^{avg}}{\sigma_a}$	Bond Strength, MPa**
0.5	0.2415	1.310	2.04	16.98	0.2136	1.350	1.99	24.52
1	0.2188	1.386	1.77	14.73	0.1987	1.402	1.75	21.56
2	0.2074	1.414	1.55	12.9	0.1843	1.391	1.50	18.48

\*Based on an average applied stress at debonding of 8.3 MPa

\*\*Based on an average applied stress at debonding of 12.3 MPa

where stress averaging is done over the same distance at which these parameters have been evaluated. It is further observed that small variations in the quantities  $\lambda$  and k obtained from FEM solution have negligible influence on the stress averaging given by Equation (3).

The tensile strength of the interface using the cruciform specimen results can be estimated by multiplying the externally applied stress with the stress concentration factor at the interface and is calculated as 23.4 MPa ( $=19.5 \times 1.2$ ). This value is significantly higher than the value of 12.1 MPa ( $=8.3 \times 1.45$ ) reported earlier [8] which was based on 2-D concentric cylinder model [14] neglecting the end effects [15,16] and size (specifically thinness) of the samples. As seen in Figure 13 the radial stress at the interface settles down to approximately 1.3 times the far-field stress ( $s_a$ ) at a sufficient distance from the fiber end for straight-sided specimens, as shown from 3-D finite element analysis. This value (1.3) is less than the value (1.45) determined using 2-D concentric cylinder analysis and can be ascribed to stress relaxation due to proximity of the specimen faces. As shown in Table 3 the stress concentration factor calculated at the exposed fiber end (for the three averaging distances considered) for straight-sided specimens is higher than the value of 1.45 used for earlier predictions, which resulted in lower estimates of the bond strength of the interface. On the other hand we have demonstrated that the cross-shaped design is successful in forcing debond initiation in the interior of the sample (region free of stress singularities), and therefore the results produced by testing of such specimens may be capable of

providing the true transverse response of the fiber-matrix interface. Comparison of the interface strength value (23.4 MPa) with the predicted strengths in Table 3 suggests that  $0.5 < z_{\text{avg}}/R < 1$  is a reasonably good distance over which stresses should be averaged to obtain an average strength of the interface that is representative of the material for straight-sided specimens with fiber ends embedded. However, for straight-sided specimens with fiber ends exposed, the predicted strength values are lower when averaged over the same distance. One of the possible causes for lower strength values is machining-induced damage during specimen preparation prior to testing. For exposed-fiber specimens, the radial stress at the interface peaks at the free edge, whereas for embedded specimens, it is at the fiber corner in the interior of the sample. These are precisely the locations where failure was found to initiate during testing of straight-sided specimens. Thus, surface damage induced during sample preparation will facilitate failure for exposed-fiber specimens and will have negligible influence on specimens with fiber ends embedded.

## 2.5 CONCLUSIONS

Careful design and testing of model composites appears to be useful in estimating the normal strength of the fiber-matrix interface in unidirectional fiber composites. Two simple specimen geometries, namely embedded fiber and cruciform design, have been considered to remove the influence of the free surfaces from tests on traditional straight-sided specimens. Results indicate good correlation between experiments and the analytical predictions and demonstrate the importance of stress-field singularities in controlling damage initiation in straight-sided samples. It is further shown that only the cross-shaped design is successful in forcing debond initiation in the interior of the sample (region free of stress singularities), and therefore the results produced by testing of such specimens may be capable of providing the true transverse response of the fiber-matrix interface.

### 3. DAMAGE MODES IN MULTIDIRECTIONAL CERAMIC-MATRIX COMPOSITES

Ceramic-matrix composites generally exhibit matrix and/or interface damage well before final failure because of the low strain capability of the brittle matrix and weak interfacial bonding. This damage has a significant influence on the stress-strain behavior as well as on the ultimate strength of the composite. The failure process in a multidirectional laminate is further complicated by its dependence on ply orientations and stacking sequence. Analytical and experimental investigations were carried out in an attempt to understand the initiation and propagation of damage in a  $[0/90]_{3S}$  cross-ply laminate. In this work a glass-ceramic matrix composite reinforced with silicon-carbide (SiC) (Nicalon) fibers was investigated at room temperature under uniaxial tensile loading. The initiation and propagation of interfacial debonding, microcracking, and fiber breaks were observed *in situ*, under applied load, using a specially-built loading device. The observed damage modes were then incorporated into existing micromechanical models to predict the laminate stress-strain behavior and compared with the experimental measurements.

#### 3.1 EXPERIMENT

The material system considered in this work was SiC fiber-reinforced glass-ceramic matrix [calcium aluminosilicate (CAS)] composites. Both unidirectional and  $[0/90]_{3S}$  cross-ply laminates were considered. The fiber volume content was determined using an image analyzing technique, and its average value for 10 measurements was found to be 41 percent with a coefficient of variation of seven percent.

Straight-sided flat specimens were then cut from the panels (2.5 mm thick) with a miniature diamond-impregnated saw using special care to minimize cutting-edge damage. The specimens were 7.6 mm wide and 100 mm long. Thin glass-fiber end tabs (25.4 mm long) were mounted on both ends of the specimen to protect them from possible gripping damage during loading. One free edge of the  $[0/90]_{3S}$  specimen was progressively ground and then polished

using successively smaller-diameter alumina polishing powder (final size was 0.3 micrometer) in order to enhance the microscopic image for crack detection. An axial strain gage (3.2 mm gage length) and a transverse strain gage were mounted on the midsurface of the specimen to monitor strain during loading.

Uniaxial tensile loading was applied to a specimen of  $[0/90]_{3S}$  laminate using a miniature loading device (hereafter referred to as strain) which was designed and built for *in situ* observation of damage in composite laminates. Axial force was generated by pulling the piston using nitrogen gas pressure. The straining stage is designed to be able to be mounted on the microscope stage for observation of microcracking under loading. The microcracks occurring in this class of brittle-matrix composites tend to close upon removal of the applied load. This closure of the microcracks makes them very difficult to detect using the microscope. The specimen was mounted on the strain stage and loaded to a prescribed level which is slightly higher than the expected first microcracking level on the microscope stage. This load was held during microscopic examination of microcracking by scanning a predetermined area in the polished free edge, and capturing the microcracks using an image analysis device. The captured images were then transferred to a digital disc for future analysis. This procedure was repeated a few times at successive incremental load levels up to final failure. The extension of microcracks, as well as their multiplication with incremental loading, was assessed by observing the subsequently captured images. The average value of crack spacing was obtained from 10 measurements for a specified load level. Two specimens of a  $[0/90]_{3S}$  laminate were monotonically loaded up to failure to obtain the entire stress-strain behavior of the laminate.

### 3.2 ANALYTICAL BACKGROUND

In this work the large radius axisymmetric damage model by Schoeppner and Pagano [17] was employed in order to approximate the thermoelastic stress field of flat laminated bodies. The model was generated by subdividing the body into regions consisting of concentric shells of constant length and satisfying Reissner's variational equation with an assumed equilibrium stress

field within each region. It has been shown that in the limit as the ratio of average cylinder radius  $R$  to laminate thickness  $T$  approaches infinity, the gradient of the hoop strain through the wall thickness approaches zero, generating a stress-strain field equivalent to a flat composite coupon under a uniform axial strain. The model can be used to examine the initiation, propagation, and interaction of various idealized damage such as delamination and transverse ply cracking in flat laminates containing orthotropic layers. It is assumed that transverse cracks are normal to the layer interface and extend the full depth of the ply. Furthermore, free-edge effects are neglected in this 2-D model.

In this work we considered the effect of transverse cracking and delamination on the extensional stiffness and Poisson's ratio of a  $[0/90]_{3S}$  cross-ply laminate. Under uniaxial strain in the  $x$ -direction, while the remainder of the external boundaries are traction free, the longitudinal stiffness,  $E_{xx}$ , and major Poisson's ratio,  $\nu_{xy}$ , are defined as:

$$E_{xx} = \frac{\bar{\sigma}_{xx}}{\bar{\epsilon}_{xx}} \text{ and } \nu_{xy} = -\frac{\bar{\epsilon}_{yy}}{\bar{\epsilon}_{xx}} \quad (4)$$

where the bar denotes the average value of the stated quantity over the unit cell, and  $\sigma_{ij}$  and  $\epsilon_{ij}$  are the stress and strain components in Cartesian coordinates, respectively. The constituent thermoelastic properties used for analytical calculations are given in Table 4.

TABLE 4  
CONSTITUENT PROPERTIES

$E_f = 200 \text{ GPa}$	$\alpha_f = 3.2 \times 10^{-6}/^{\circ}\text{C}$
$E_m = 100 \text{ GPa}$	$\alpha_m = 5.0 \times 10^{-6}/^{\circ}\text{C}$
$\nu_f = \nu_m = 0.25$	

It is assumed that each constituent is isotropic. Further,  $E$  represents Young's modulus,  $\nu$  the Poisson's ratio, and  $\alpha$  the coefficient of thermal expansion (CTE), whereas subscripts  $f$  and  $m$  refer the stated quantities to fiber and matrix, respectively. The process temperature difference,  $\Delta T$ , is assumed to be  $-600^{\circ}\text{C}$ .



### 3.3 RESULTS

#### 3.3.1 Elastic Properties

The elastic properties of the unidirectional ply were calculated from the constituent properties using the NDSANDS model developed by Pagano and Tandon [14]. Comparison of the initial elastic moduli between calculation and experiment is summarized in Table 5.

TABLE 5  
ELASTIC PROPERTIES OF UNIDIRECTIONAL LAMINATE

Property	Theory	Experiment
Longitudinal modulus, GPa	140	134
Transverse modulus, GPa	130	123
Major Poisson's ratio	0.25	0.25

These ply properties are used for subsequent prediction of elastic constants of the  $[0/90]_{3S}$  laminate using classical laminated plate theory. The experimental results are compared with the analytical prediction given in Table 6.

TABLE 6  
ELASTIC PROPERTIES OF  $[0/90]_{3S}$  LAMINATE

Property	Theory	Experiment (Cv)
Elastic modulus, GPa	135	117 (4.1)
Poisson's ratio	0.24	0.20 (12.5)

Cv: coefficient of variation, %

The measured modulus is observed to be lower compared to the theoretical predictions (assuming no damage is present) indicating that there could be some processing-induced initial damage in the cross-ply laminate.

### 3.3.2 Damage Progression

The damage progression in the form of matrix cracking was assessed under incremental loading. The microcracks were found to be initiated in the 90° layers as a partial debond at the interface between fiber and matrix before branching into the matrix as shown in Figure 15. These microcracks propagate almost at once across the entire width of the 90° ply and link up with neighboring plies as the applied stress increases. Figure 16 shows an increase in transverse crack development in the laminate at four increasing loads. Crack spacing between two neighboring cracks also decreases as stress level increases and appears to reach a saturation value (0.0081 mm) before final failure. Damage mechanisms such as interface debonding, matrix cracking, and fiber fracture are responsible for the nonlinear stress-strain behavior and continuous degradation of laminate properties.

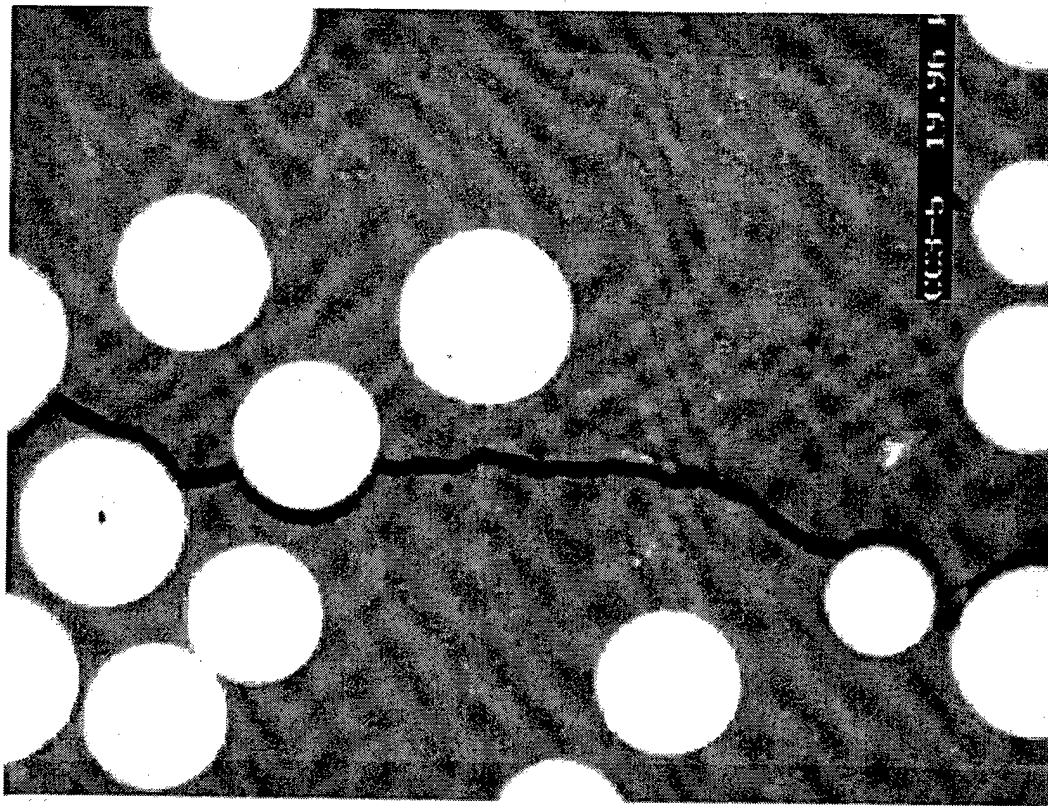


Figure 15. Photomicrograph Showing Partial Debonding of Fiber Matrix Interface and Extending into Matrix.

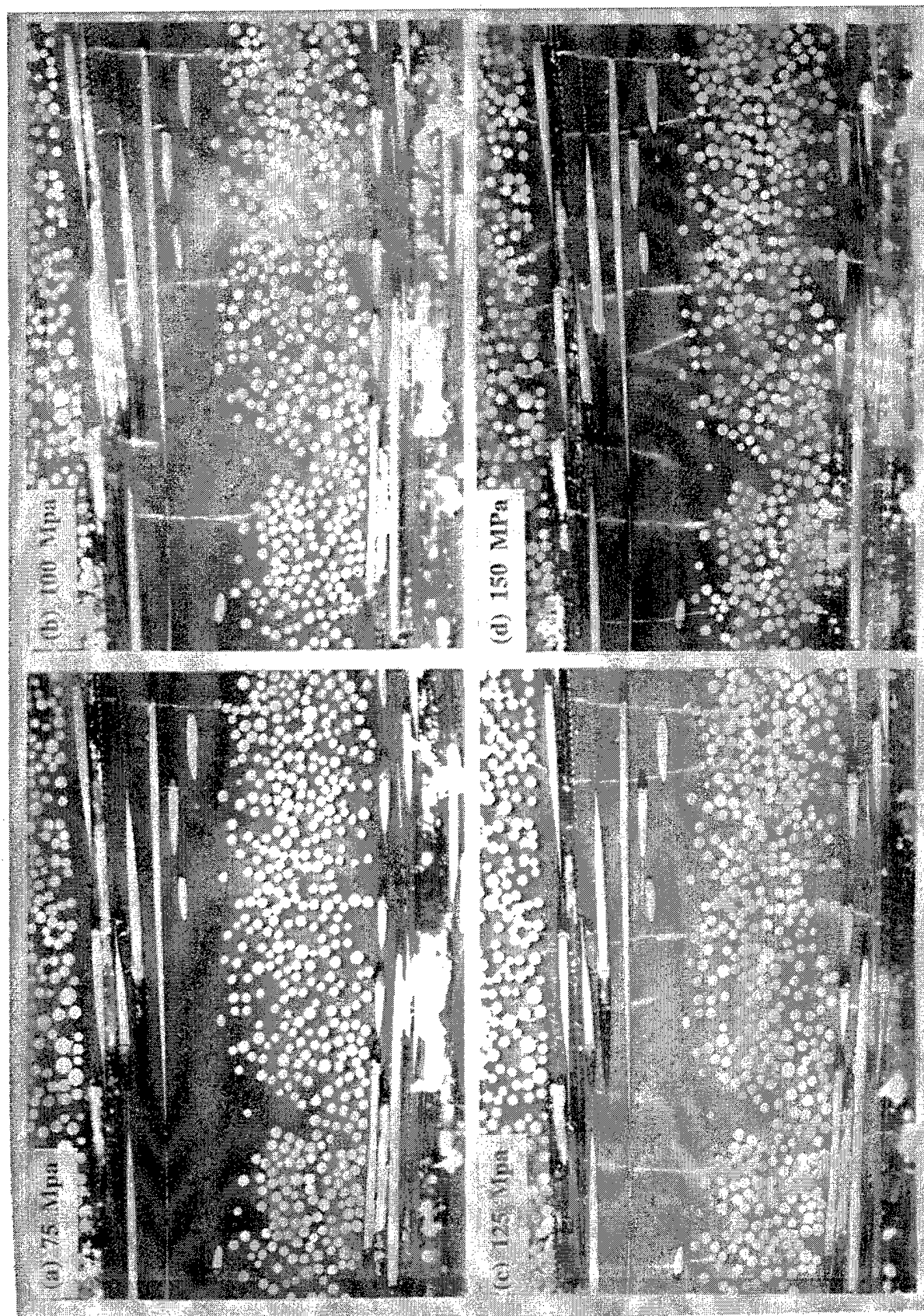


Figure 16. Photomicrograph Showing Damage Progression for a  $[0/90]_{3s}$  Laminate Specimen.

### 3.3.3 Stress-Strain Behavior

Figure 17 shows typical axial and transverse stress-strain relations for the  $[0/90]_{3s}$  laminate. The axial stress-strain behavior is seen to be linear both in its initial and final stages while becoming nonlinear in the transition stage. The transverse strain varies nearly linearly up to 138 GPa and thereafter reverses its direction until final failure. This reversal of the transverse strain occurs in the nonlinear region of the axial stress-strain relation. Figure 18 shows variation of major Poisson's ratio as a function of applied stress. The Poisson's ratio decreases drastically in the transition region of the stress-strain curve (Figure 17) where the transverse strain reversal occurred.

Based on the observed progression of damage, we now assume the following idealized damage states and calculate the axial modulus ( $E_{xx}$ ) and Poisson's ratio  $\nu_{xy}$  using the large radius axisymmetric model [17].

Stage of Damage State	$E_{xx}$ , GPa	$\nu_{xy}$
1. No damage present.	135	0.24
2. Complete debonding of fiber/matrix interface in all $90^\circ$ plies.	91	0.16
3. Transverse cracking of all $90^\circ$ plies in conjunction with damage stage 2 (crack spacing 0.0081 mm).	72	0.13
4. Transverse cracking of either of inner two $0^\circ$ plies in conjunction with damage stage 3.	50.5	0.08
5. Transverse cracking of all plies except outer two $0^\circ$ plies.	25.2	0.04
6. Extension of axial crack (crack length 0.0081 mm) from the tip of the transverse cracks in damage stage 5.	24.5	0.04

The predicted values of  $E_{xx}$  and  $\nu_{xy}$  compare favorably with the experimental results in the initial linear region (stage 1) and final (stages 5 and 6) linear regions. In the nonlinear transition region (stages 2-4), we are unable to directly compare the predictions with experiment because of the inability to distinguish the corresponding damage stages in the present

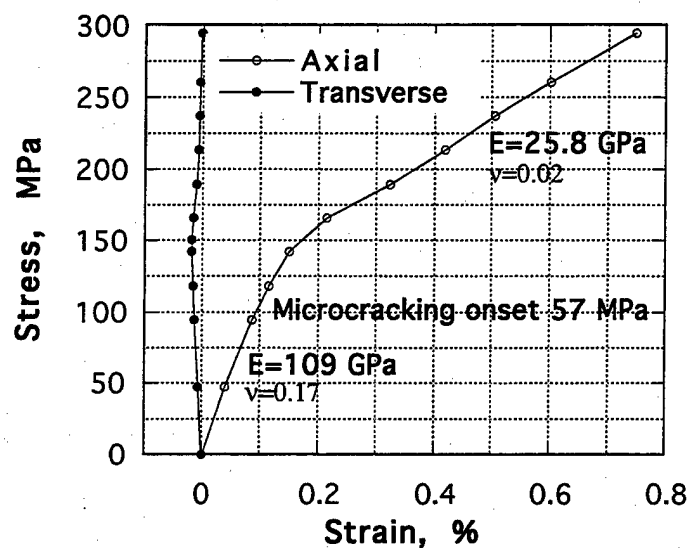


Figure 17. Stress-Strain Relation for the  $[0/90]_{ss}$  Laminate at Room Temperature.

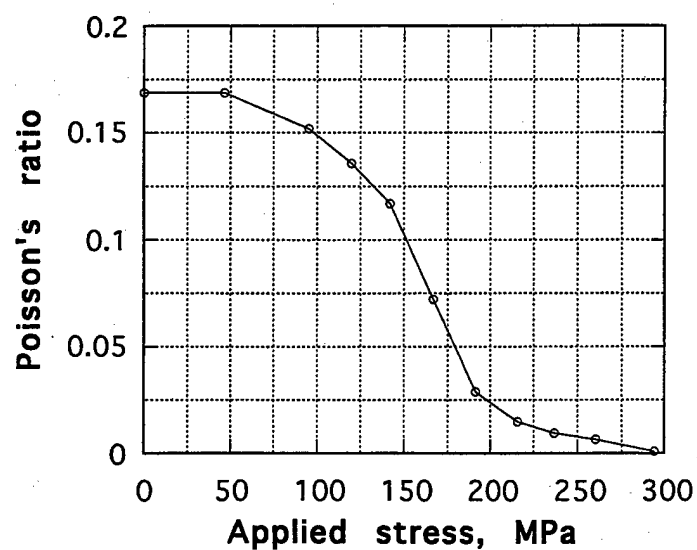


Figure 18. Experimentally-Measured Major Poisson's Ratio as a Function of Applied Stress for  $[0/90]_{ss}$  Laminate at Room Temperature.

experiment. Further work is in progress to identify and capture the growth of dominant damage mechanisms with incremental loading in the transition region.

### **3.4 SUMMARY**

The initiation and progression of damage in the  $[0/90]_{3S}$  laminate of SiC fiber- (Nicalon) reinforced glass-ceramic matrix (CAS) composite have been investigated under uniaxial tension. Damage mechanisms in the form of fiber/matrix interface debonding, matrix cracking, and longitudinal splitting are assessed at each incremental loading. Based on the observed damage states, analytical calculations were made to predict change in modulus and Poisson's ratio corresponding to the idealized states of damage. The correlation between analytical prediction and experimental results is promising.

## 4. MEASUREMENT OF ELASTIC MODULI OF FIBER COATINGS

### 4.1 EXPERIMENT

A nanoindentation experiment was conducted to measure the *in situ* elastic modulus of fiber coatings. The material system studied in this work was borosilicate matrix composite reinforced with SiC fibers. The SiC fiber has two coatings of carbon and TiB<sub>2</sub>. The thickness of the carbon layer is ~1.5 μm and that of the TiB<sub>2</sub> layer is ~0.5 μm. Two types of indentation surfaces, 15° and 90° with respect to fiber direction, were prepared. The indentation surface was progressively ground and then polished using smaller diameter alumina polishing powder (final size was 0.3 micrometer) in order to obtain a microscopically even indentation area.

Depth-sensing indentation (DSI) tests were conducted in the displacement control mode using a Berkovitch indenter. Figure 19 illustrates a typical load-displacement curve from a DSI test. The elastic modulus (E) was calculated from the load-displacement plots using Equation (5) which was derived from the elastic punch model of Sneddon [18]

$$\left( \frac{1-\nu^2}{E} + \frac{1-\nu_o^2}{E_o} \right) \frac{dp}{dh} = 2\sqrt{\frac{A_c}{P}} \quad (5)$$

where  $dp/dh$  is the initial slope of the unloading segment (Figure 19),  $\nu$  and  $\nu_o$  are the Poisson's ratios, and  $E$  and  $E_o$  are the elastic moduli for the specimen and the indenter material, respectively.  $P$  and  $A_c$  are the applied load and contact area, respectively. The Poisson's ratio was assumed to be 0.25 for fiber, coatings, and matrix.

A total of 160 indentations and 300 indentations were conducted on two fibers in a 90° surface and on three fibers in a 15° surface, respectively. Two different indentation forces applied were 0.005 N and 0.01 N with a 0.5-micrometer interval. Indented marks are identified under SEM.

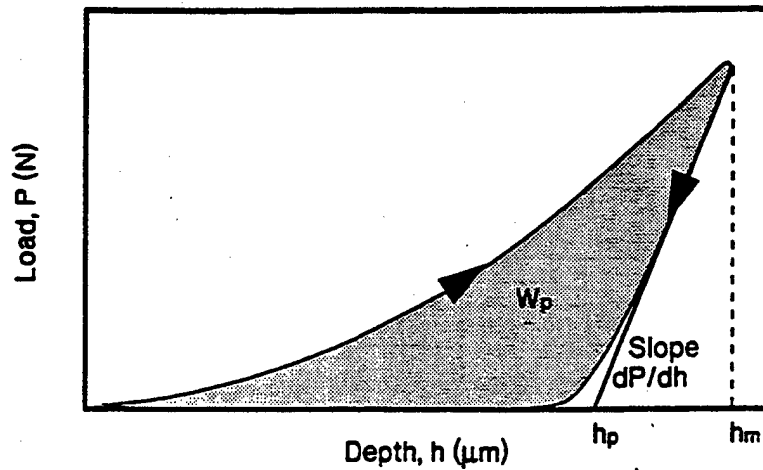


Figure 19. Typical Load-Displacement Curve from a DSI Test.  $dp/dh$  is the slope of the initial linear portion of the unloading segment.

## 4.2 RESULTS

After tests, specimens were examined under SEM to identify all indentation locations. A series of indentations on the  $90^\circ$  surface are shown in Figure 20. Indentations are vaguely seen in coating layers. Figures 21a-d show a typical load-displacement curve for fiber, C-layer,  $\text{TiB}_2$  layer, and matrix. Table 7 summarizes the test results. Data reduction was performed on 197 tests as shown in Table 7. All test data on the coatings are included.

The average elastic moduli values obtained for the fiber and matrix appear to be independent of indent loads of 0.005 N and 0.01 N, and are slightly higher for a  $15^\circ$  surface. These values are comparable to the results (352 GPa for fiber and 62 GPa for matrix) obtained by Berriche [19]. The average elastic moduli measured on the  $90^\circ$  surface are considerably greater than the values on the  $15^\circ$  surface for both C-layer and  $\text{TiB}_2$  layer as shown in Table 7. The average values measured on the  $15^\circ$  surface are 73 GPa and 151 GPa for C-layer and  $\text{TiB}_2$  layer, respectively, and are comparable to the results (91 GPa for C-layer and 143 GPa for  $\text{TiB}_2$  layer) of Berriche. Further testing needs to be done to understand the difference in coating modulus between the  $90^\circ$  and  $15^\circ$  surfaces. For a very thin layer coating like the  $\text{TiB}_2$  layer, the increase



TABLE 7  
SUMMARY OF TEST RESULTS

	Force N	90° Surface			15° Surface		
		Modulus, GPa	STD	No. of Tests	Modulus, GPa	STD	No. of Tests
Fiber	0.005	387.3	15.0	14	417.8	4.7	6
	0.010	393.8	15.5	16	402.0	10.7	42
C-layer	0.005	117.3	10.5	3	70.5	7.8	11
	0.010	116.9	10.5	3	75.1	11.0	21
TiB <sub>2</sub> -layer	0.005	239.9	25.2	3	156.9	17.3	6
	0.010	280.7	46.7	2	145.0	6.9	3
Matrix	0.005	61.5	1.5	14	64.4	1.7	23
	0.010	61.7	2.2	23	68.4	1.3	7

STD: Standard deviation

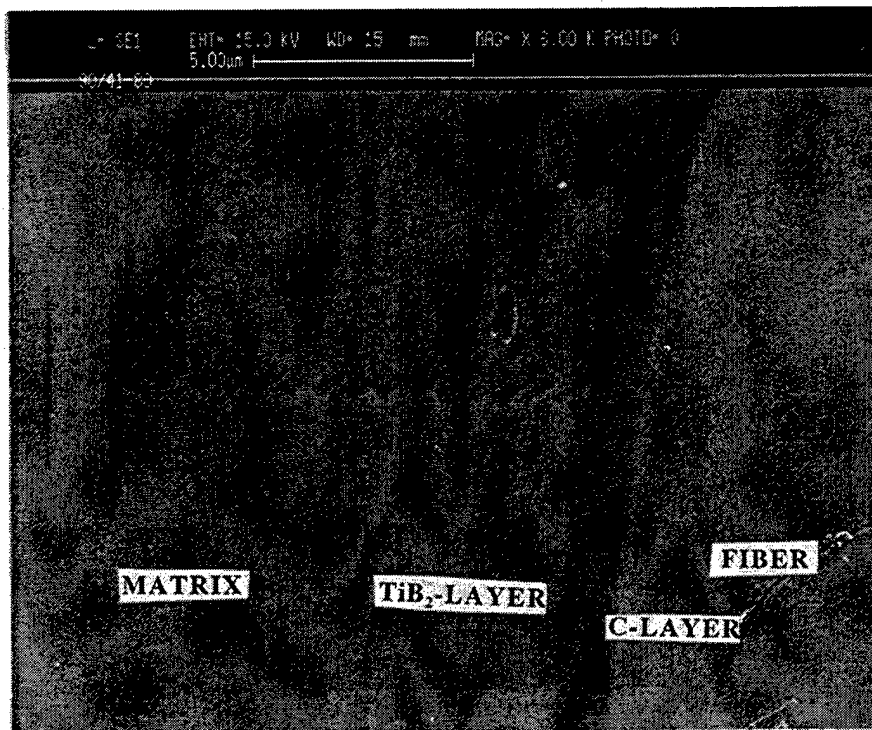
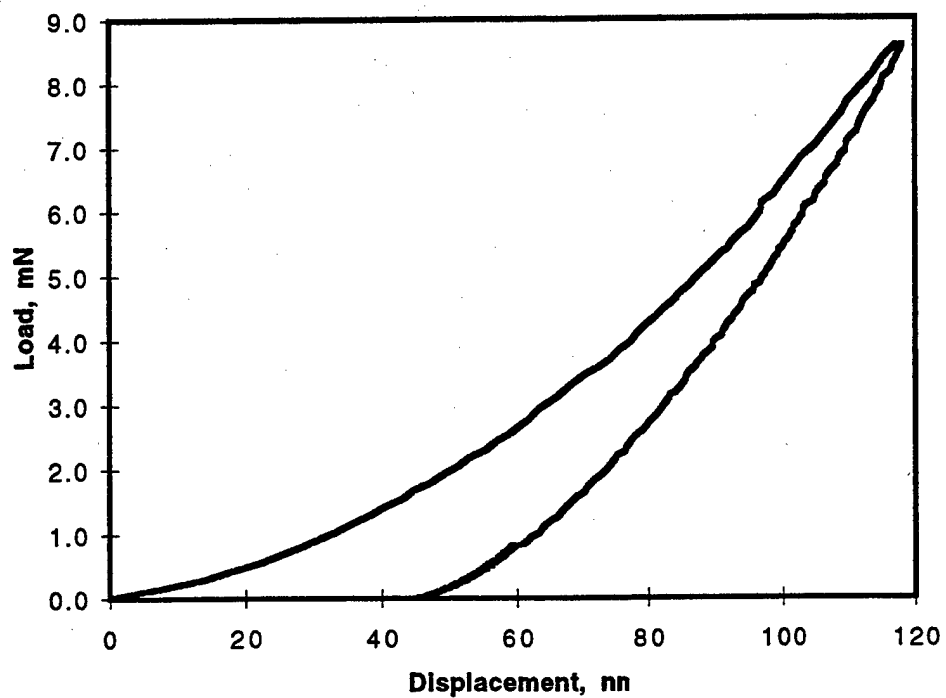
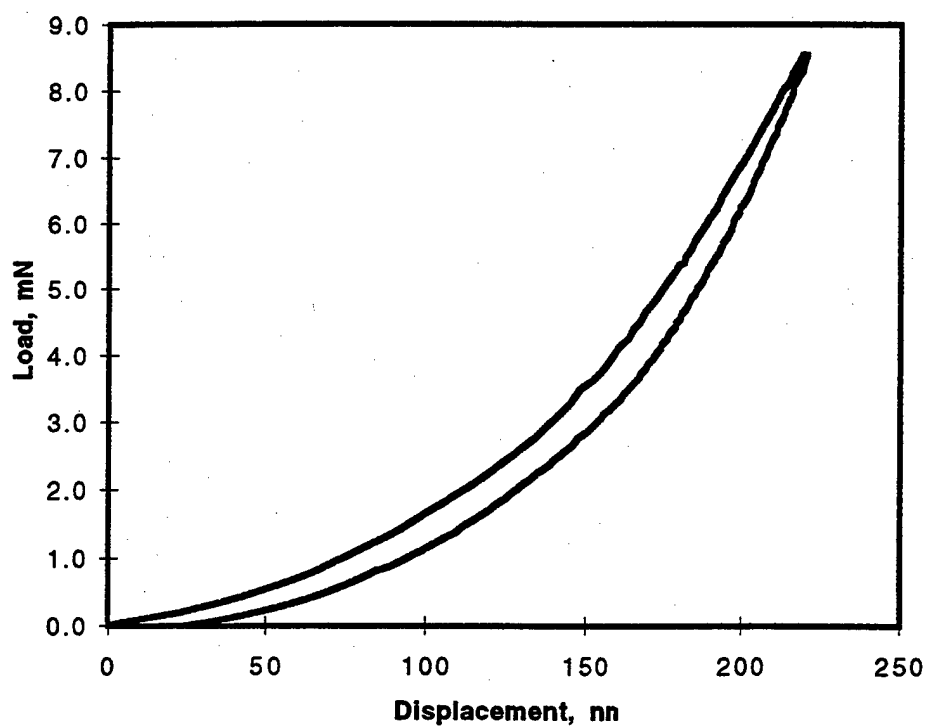


Figure 20. Micrograph Showing a Series of Indentations on the 90° Surface.



(a)



(b)

Figure 21. Load vs. Displacement on the 90° Surface: Applied Load = 10 mN.  
(a) Fiber; (b) c-Layer; (c) TiB<sub>2</sub>-Layer; (d) Matrix

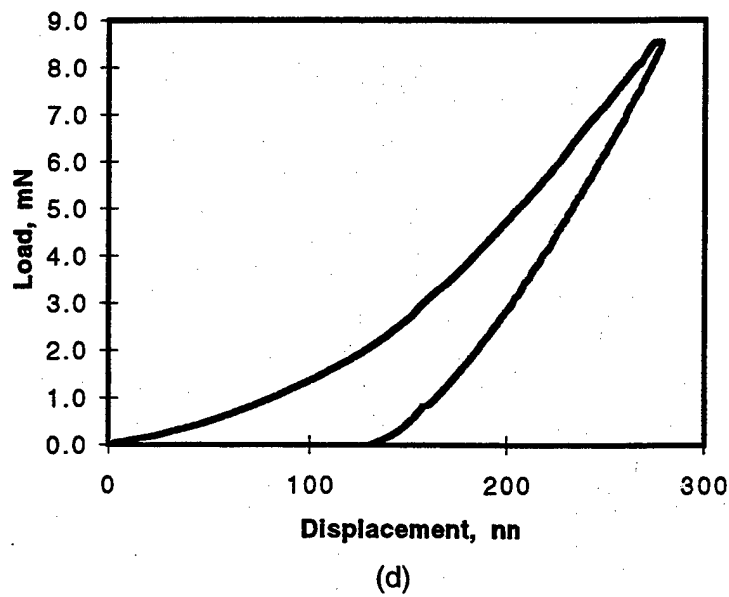
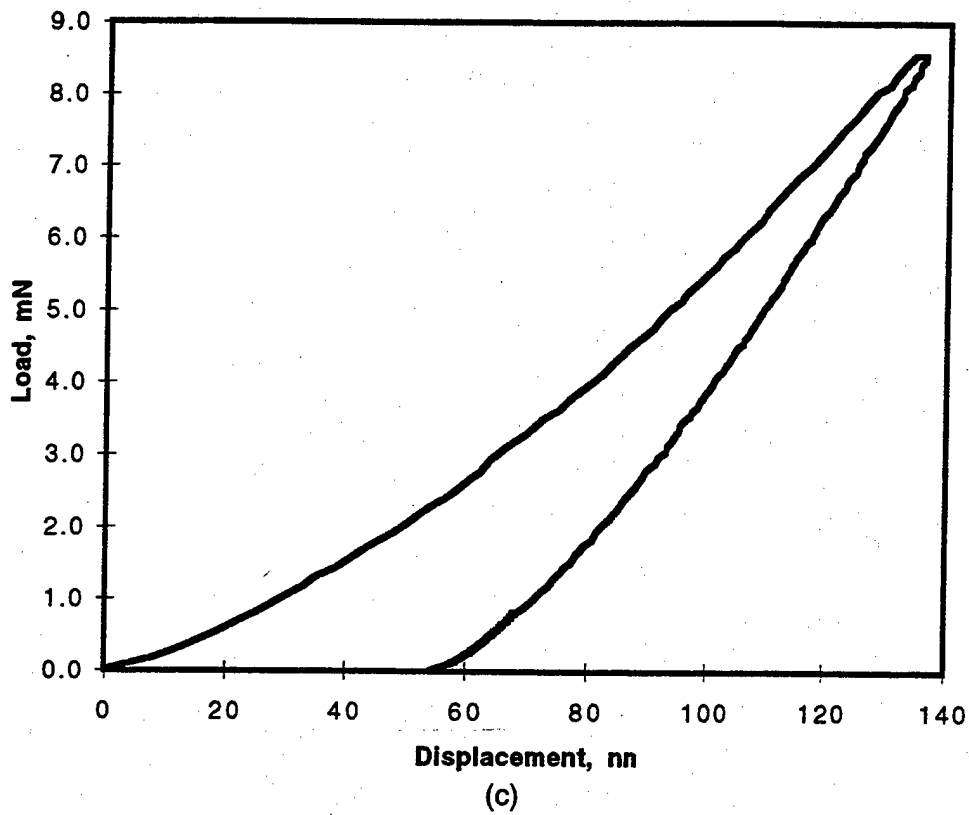


Figure 21. (Concluded). Load vs. Displacement on the  $90^\circ$  Surface: Applied Load = 10 mN.  
 (a) Fiber; (b) c-Layer; (c)  $\text{TiB}_2$ -Layer; (d) Matrix

of the indent surface by a low-angle cutting gives a better chance of indenting the exact area of interest and a reliable value. Although the test results appear to compare reasonably well with the published results, further work is needed to gain confidence and reliability in this test.

## 5. CONCLUSIONS AND RECOMMENDATIONS

### 5.1 CRACK INITIATION IN BRITTLE-MATRIX COMPOSITES

- There is a strong correlation between the analytical model and experimentally-measured composite cracking stress for composites with both a continuous interface and a sliding frictionless interface.
- For composites where  $a_m > a_f$ , the matrix cracking stress increases with fiber volume fraction but decreases as the tensile axial residual stress increases.
- For composites where  $a_m < a_f$ , the experimentally-determined matrix cracking stresses were lower than those predicted by the model, possibly due to partial debonding during processing.
- The matrix cracking stress increased in composites with small-diameter, uniformly-spaced fibers and a strong interface.
- Future work will address composite cracking stresses of composites reinforced with fibers that do not have an outer carbon layer but yet bond strongly to the matrix.

### 5.2 NORMAL STRENGTH IN MODEL UNIDIRECTIONAL COMPOSITES

- The normal strength of the fiber-matrix interface in unidirectional composites can be estimated from tests on model composites.
- The free-edge effect with the traditional specimen can be eliminated by using either embedded fiber end or cross-shaped specimen geometry.
- A good correlation exists between experiments and analytical predictions of transverse strength.

- The importance of stress field-singularities was demonstrated in controlling damage initiation in straight-sided specimens.
- The cruciform design appears to be capable of providing the true transverse response of the fiber-matrix interface.
- Future work will address measurement of transverse strength using composites with multiple fibers.

### **5.3 DAMAGE MODES IN MULTIDIRECTIONAL CERAMIC-MATRIX COMPOSITES**

- Damage modes observed are interface debonding, matrix cracking and fiber breakage.
- Damage initiation occurred in the 90° plies through interfacial debonding which propagated into the matrix.
- Significant changes were observed in composite modulus and Poisson's ratio as damage progressed.
- A good correlation exists between the analytical prediction and experimental results on modulus and Poisson's ratio corresponding to various states of damage.
- Axial cracking (interfacial debonding and delamination between plies) has little influence on the modulus.
- Future work will address the effect of temperature on the damage initiation and propagation, and the corresponding stress-strain behavior.

### **5.4 MEASUREMENT OF ELASTIC MODULI OF FIBER COATINGS**

- The elastic moduli of very thin fiber coatings can be measured using depth-sensing indentation tests.

- Although the test results appear to compare reasonably well with the published data, further work is needed to gain confidence in the reliability of this test.

## 6. PUBLICATIONS/PRESENTATIONS

Kim, R. Y., & N. J. Pagano. (1995, November). *Progressive Microcracking in Unidirectional SiC/CAS Composite at Elevated Temperatures*. Presented at ASME Winter Meeting, San Francisco, CA.

Matikas, T. E., P. Karpur, R. Dutton, & R. Kim. (1995). Influence of the Interface and Fiber Spacing on the Fracture Behavior of Glass Matrix Composites. *Materials Evaluation* 53(5).

Dutton, R. E., N. J. Pagano, & R. Y. Kim. (1996). Influence of Residual Stress and Interface Bonding on Matrix Cracking Stress and Ultimate Strength of Borosilicate Glass-SiC Fiber Composites. *J. Amer. Cer. Soc.*

Tandon, G. P., & R. Y. Kim. (1996). Test Methods for Estimation of Interfacial Normal Strength in Unidirectional Fiber Reinforced Composites. *Proc. of the American Society for Composites* 11 (pp 897-905).

Tandon, G. P., R. Y. Kim, & R. E. Dutton. (1996, November). *Micromechanical Edge Effects in Glass Matrix Composites*. Paper presented at ASME Winter Meeting, Atlanta, GA.

Tandon, G. P., R. Y. Kim, & R. E. Dutton. (1977). Failure Modes in Unidirectional Composites Under Transverse Loading. *J. of Reinf. Plas. & Compos.* 16(1) (pp. 33-49).

Tandon, G. P., R. Y. Kim, S. G. Warrier, & B. S. Majumdar. (1997, October). *Influence of Edge Effects in Estimating Interfacial Normal Strength in Model Unidirectional Composites*. To be presented at American Society for Composites Annual Meeting, Dearborn, MI.

Kim, R. Y., & G. P. Tandon. (1997, November). *In Situ Observation and Modeling of Damage Modes in Cross-Ply Ceramic Matrix Composites*. To be presented at ASME Winter Meeting, Dallas, TX.

Pagano, N. J., R. Dutton, & R. Y. Kim. (1998, January). *Ultimate Tension Failure of Borosilicate-SiC Fiber Unidirectional Composites*. To be presented at American Ceramic Society Meeting, Cocoa Beach, FL.



## 7. REFERENCES

1. Pagano, N. J., & R. Y. Kim. (1994). Progressive Microcracking in Unidirectional Brittle Matrix Composites. *Mech. Comp. Mat. Struc.* 1(1) (3-29).
2. Pagano, N. J., & R. Y. Kim. (1995, June). *Progressive Fracture Modes in a Brittle Matrix Composite Under Tension*. Presented at ASME Symposium on Composites, Santa Monica, CA.
3. Berriche, R., & R. E. Dutton. (1995). Elastic Moduli of  $TiB_2$  and C Layers in a Fiber Reinforced Glass Ceramic Matrix. *Scripta Met.* 33(5) (789-794).
4. Gustafson, C. M., R. E. Dutton, & R. J. Kerans. (1995). Fabrication of Glass Matrix Composites by Tape Casting. *J. Am. Ceram. Soc.* 78(5) (1423-24).
5. Pagano, N. J., & H. W. Brown, III. (1993). The Full-Cell Cracking Mode in Unidirectional Brittle Matrix Composites. *Composites* 24(2) (69-83).
6. Pagano, N. J. (1992). Axisymmetric Stress Fields in Composites. In J. N. Reddy and K. F. Reifsnider, eds., *Local Mechanics Concepts for Composite Material Systems*. Berlin: Springer-Verlag.
7. Kim, Ran Y., & N. J. Pagano. (1991). Crack Initiation in Unidirectional Brittle-Matrix Composites. *J. Am. Ceram. Soc.* 74(5) (1082-90).
8. Tandon, G. P., & R. Y. Kim. (1997). Test Methods for Estimation of Interfacial Normal Strength in Unidirectional Fiber Reinforced Composites. To be published in *Journal of Reinforced Plastics and Composites*.
9. Shoufeng, H., P. Karpur, T. E. Matikas, L. Shaw, & N. J. Pagano. (1996). Free Edge Effect on Residual Stresses and Debond of a Composite Fiber/Matrix Interface. To appear in *Mechanics of Composite Materials and Structures*.
10. Tandon, G. P., R. Y. Kim, & R. E. Dutton. (1996, November). *Micromechanical Edge Effects in Glass Matrix Composites*. Presented at ASME IMECE, Atlanta, GA.
11. Gundel, D. B., B. S. Majumdar, & D. B. Miracle. (1995). Evaluation of the Transverse Response of Fiber-Reinforced Composites Using a Cross-Shaped Sample Geometry. *Scripta Metallurgica et Materialia* 33 (2057-65).

12. Warrier, S. G., D. B. Gundel, B. S. Majumdar, and D. B. Miracle. (1996). Interface Effects on the Micromechanical Response of a Transversely Loaded Single Fiber SCS-6/Ti-6Al-4V Composite. *Metal. Mater. Trans.* 27A (2035-43).
13. Bogy, D. B. (1991). Two Edge Bonded Elastic Wedges of Different Materials and Wedge Angles Under Surface Traction. *J. Appl. Mech.* (377-386).
14. Pagano, N. J., & G. P. Tandon. (1988). Elastic Response of Multidirectional Coated Fiber Composites. *Composites Sci. and Tech.* 31 (273-293).
15. Kroupa, J. L., & N. E. Ashbaugh. (1995). Stress-Free Edge Effects on the Transverse Response of a Unidirectional Metal Matrix Composite. *Composites Engineering* 5 (569-582).
16. Folias, E. S. (1989). On the Stress Singularities at the Intersection of a Cylindrical Inclusion with the Free Surface of a Plate. *Int. J. Fracture* 39 (25-34).
17. Schoeppner, G. A., & N. J. Pagano. (1997). Stress Fields and Energy Release Rates in Cross-Ply Laminates. To be published in *Int. J. of Solids and Structures*.
18. Sneddon, I. A. (1965). The Relation between Load and Penetration in the Axisymmetric Boussinesq Problem for a Punch of Arbitrary Profile. *Int. J. Eng. Sci.* 3.
19. Berriche, R. (1995, February). *Elastic Moduli of TiB<sub>2</sub> and C Layers in a Fiber Reinforced Glass Ceramic Composite* (LTR-ST-1998). Canada: Institute for Aerospace Research, NRC.